THEORETICAL MODELING OF DEFECT CENTERS IN SELECTED MINERALS

A Thesis Submitted to the College of

Graduate Studies and Research

in Partial Fulfillment of the Requirements

for the Degree of Doctor of Philosophy

in the Department of Geological Sciences

University of Saskatchewan

Saskatoon

By

Sanda M. Botis

Permission to use

In presenting this thesis in partial fulfilment of the requirements for a Doctor of Philosophy degree from the University of Saskatchewan, I agree that the Libraries of this University may make it freely available for inspection. I further agree that permission for copying of this thesis in any manner, in whole or in part, for scholarly purposes may be granted by the professor or professors who supervised my thesis work or, in their absence, by the Head of the Department or the Dean of the College in which my thesis work was done. It is understood that any copying or publication or use of this thesis or parts thereof for financial gain shall not be allowed without my written permission. It is also understood that due recognition shall be given to me and to the University of Saskatchewan in any scholarly use which may be made of any material in my thesis.

Requests for permission to copy or to make other use of material in this thesis in whole or part should be addressed to:

Head of the Department of Geological Sciences
University of Saskatchewan
114 Science Place
Saskatoon, Saskatchewan
S7N5E2, Canada

Abstract

This thesis presents *ab-initio* quantum mechanical calculations at the density functional theory (DFT) level on defect centers hosted by crystalline systems of geologic importance (i.e. fluorite, quartz, stishovite). The research brings new, complementary data to the current understanding of defect structures in minerals and explores the advantages of a theoretical approach in the field of mineral spectroscopy.

This present research presents the first *ab-initio* calculations of the O_2^{3-} type defects in crystalline solids. New data on the electronic properties and structural characteristics of O_2^{3-}-Y^{3+} defect in fluorite-type structures (CaF_2 and SrF_2) were obtained at the DFT level. These results confirm the stability and the molecular character of the O_2^{3-}-Y^{3+} center, revealing a spin density that is equally distributed between the two oxygen atoms. Our results report an O-O bond distance of 2.47 Å in CaF_2 and 2.57 Å in SrF_2. The calculated ^{17}O and ^{19}F hyperfine constants for of the O_2^{3-}-Y^{3+} center are in good agreement with their corresponding experimental values reported by previous electron paramagnetic resonance (EPR) and electron nuclear double resonance (ENDOR) studies, while discrepancies are notable for the ^{89}Y hyperfine constants and are probably attributable to an inadequate basis set for Y.

The present study provides a more complete picture of the coupled Al-M substitution for Si in quartz, while investigating the characteristics and electronic properties of the diamagnetic $[AlO_4/M^+]^0$ (where M = H, Li, Na and K) defects. The diamagnetic

$[AlO_4/M^+(a_<)]^0$ defects with M = H, Li and Na have been shown to be more stable than their $[AlO_4/M^+(a_>)]^0$ structural analogues (where $a_>$ and $a_<$ denote the location of the charge compensating ion on the long-bond and short-bond side, respectively), correctly predicting the common occurrence of paramagnetic $[AlO_4/M^+(a_>)]^+$ centers. The present study confirms previous suggestions that incorporation of the $[AlO_4/M^+]^0$ defects results in significant structural relaxations that extend at least to the nearest Si atoms. The $[AlO_4/K^+]^0$ defects have been investigated for the first time and are shown to be stable in quartz. The results of this study have implications for the uptake of Al in quartz.

The present research evaluates the structural models of $[AlO_4/Li]$ paramagnetic defects in α-quartz. The results confirm the previous experimental findings and propose an additional paramagnetic defect $[AlO_4/Li^+(c_{small})]^+$, with the unpaired electron located on a short-bonded O atom and the Li compensator just off the edge of the small channel. Accordingly we suggest that three distinct Al-Li paramagnetic defects can be can be found in quartz, two of them having the hole located on a short-bonded O and one trapping the hole on a long-bonded O atom. However the structural similarities with the $[AlO_4/Li^+(a_>)]^+$ defect would require detection and measurement of the ^{17}O hyperfine structure for an unequivocal EPR identification.

The present work also reports on first-principles quantum-mechanical calculations on the previously proposed $[O_2^{3-}\text{-}Al^{3+}]$ defect in stishovite. Our results show that the unpaired spin is 85% localised on one of the six oxygen atoms at an AlO_6 octahedron, while the calculated ^{27}Al hyperfine constants are similar to those determined by EPR experiments. Accordingly we propose the Al center to represent an $[AlO_6]^0$ defect, and hole hoping among equivalent oxygen atoms is responsible for its detection only at cryogenic

temperatures. Theoretical calculations also show that diamagnetic precursors $[AlO_6/H^+]^0$, $[AlO_6/Li^+]^0$ and $[AlO_6/Na^+]^0$ are stable in stishovite. The calculated OH bond distance and orientation are in excellent agreement with those inferred from FTIR spectra and previous theoretical calculations. The calculated $[AlO_6/Li^+]^0$ and $[AlO_6/Na^+]^0$ defects suggest that monovalent cations such as Li^+ and Na^+ are potentially important in accommodating Al in stishovite in the lower mantle.

Acknowledgements

This research would have never been carried if not for my supervisor, Dr. Yuanming Pan. He inspired me to have big dreams and taught me that in science there are no limits. I would like to thank him for the time and advice that he generously gave me all these years and his way of making me understand that I already have the answers.

I would also like to express my gratitude to my friend Davy Adriaens, who supported me through the painful process of learning computer modeling. Many thanks to Dr. Furio Cora, who generously helped me with advice and our collaboration allowed me to expend my knowledge of computational modeling.

I wish to thank my entire family and friends for their support and encouragement. They have always been there for me, more proud of my achievements than I usually am. But most of all, I would like to thank my husband for the countless moments in which he had to learn about my projects, my new ideas and my problems. While my supervisor was mostly aware of the glamorous side of my research (i.e. results and interpretations), my husband had to go through all the painful cluster crashes and Linux problems. He was there to listen to me and probably never imagined how handy his degree in Physics would come in his marriage. Thank you!

TABLE OF CONTENTS

LIST OF TABLES

LIST OF FIGURES

Chapter 1

Introduction

Inevitably present in all systems, defect centers have gained their recognition as major players in determining the properties of the solid-state. Arising from both chemical substitution and as a result of natural irradiation, the presence of defect centers in minerals has applications in various areas of research from material sciences to archeology, geochronology, nuclear waste disposal and mineral exploration (Ikeya, 1993; Rossman, 1994; Marfunin, 1995; Rink, 1997; Pan et al., 2006).

The study of defect centers gained tremendous momentum especially after the realization that many properties of solids are controlled not so much by the structure of the material itself, but by the faults and defects in the structure (Tilley, 1987).

The importance of point defects in altering the physical properties of their hosts was first recognized in alkali halides with the discovery of the F_A center and its influence on the optical properties of KBr (Petroff, 1950; Seidel, 1961). Around the same time, Teal and Little (1950) in their effort to create a better transistor, pioneered the idea of doping synthetic single crystals of germanium in a precise fashion with the purpose of manipulating their electronic properties. Presently, controlling the type and concentration of defects in a material so as to tune its properties in a desired manner is employed both

in semiconductor and solid state laser technology. These simple and yet elegant ideas and the tremendous progresses done in understanding the changes in physical properties of materials as a result of defect center incorporation, have helped to create an entirely new field of research, namely defect engineering.

The research related to defect centers is not only limited to the study of optical and electronic properties. In the last few decades, properties such as diffusion, creep, elasticity, and stability of minerals at high temperature and pressure have been shown to depend on the presence of point defects (Marfunin 1995; Regenauer-Lieb et al. 2006). As an example, the study of water incorporation (i.e. hydrogen-related defects) in nominally anhydrous minerals and its effect on the petrological and geochemical evolution of the mantle is one of the most intriguing subjects in mineral physics for the last twenty years (Bell and Rossman, 1992; Ingrin and Skogby, 2000).

Moreover, the extensive occurrence of defect centers in minerals as a result of natural irradiation led to their use as natural dosimeters, geothermometers and geochronometers (Ikeya, 1993). Being able to identify the type of defect centers with their particular production and annealing rates as a function of radiation dose and temperature has made possible their use as markers of past geological events (Ikeya, 1993; Pan et al., 2006).

Consequently, the fundamental understanding of the structural characteristics, electronic properties and dynamics of defect centers is essential from two main scientific perspectives: 1) their fundamental influence on the physical properties of the host mineral, and 2) their use as tracers of past geologic conditions (i.e. irradiation, temperature, pressure, chemical heterogeneities).

1.1 Study overview

The study of point defects lies at the boundary between chemistry, physics, material sciences and mineralogy, and makes use of analytical methods and principles pertaining to all these fields. Spectroscopic methods such as optical absorption spectroscopy, infrared (IR) and Raman spectroscopy, Mössbauer spectroscopy, nuclear magnetic resonance (NMR), electron nuclear double resonance (ENDOR), electron paramagnetic resonance (EPR), to mention just a few, are generally employed in the study of defect centers. Nonetheless, EPR spectroscopy is the method that has been proven to be the most effective, due to its extremely high sensitivity (detection limit of 10^{11} unpaired spins per cubic centimeter of sample (Weil et al. 1994)) and its ability to provide detailed information on the local geometry and electronic structure of paramagnetic species. With an unparalleled sensitivity up to 10,000 times that of optical absorption spectroscopy (Rossman, 1994) EPR has emerged as the method of choice in the study of defect centers. In principle, the only limitation of EPR arises from its ability to detect only paramagnetic species, all the diamagnetic entities being EPR-silent. However this problem is easily overcome due to the fact that most defect centers are paramagnetic or can become paramagnetic as a result of irradiation.

In practice however, and particularly in the case of geological research, additional limitations of EPR spectroscopy arise as a result of both the complexity of natural samples and the simultaneous presence of magnetically similar defect centers. Therefore, EPR data obtained from minerals (and other natural materials) can often be difficult to interpret unambiguously (Botis et al., 2005; Nilges et al., 2008). A relevant example is the case of charged di-oxygen species, (i.e. O_2^+, O_2^-, and O_2^{3-}). Although paramagnetic

and studied in detail by electron paramagnetic resonance (EPR) spectroscopy (Che and Tench 1983; Murphy and Chiesa 2004), the great similarity between O_2^- and O_2^{3-} structural models makes their identification problematic (e.g., O_2^--Al^{3+} vs. O_2^{3-}-Al^{3+}, Nilges et al 2008). As a result, the structural model and magnetic properties of O_2^{3-} are poorly understood and questions remain about its bond distance and molecular character (Requardt and Lehmann 1985).

Additionally, even when the interpretation of the EPR data can be made with a very high degree of confidence, choosing between two magnetically equivalent structural models based solely on the EPR parameters can become an impossible task (Walsby et al., 2003; Botis et al., 2008). A relevant example is portrayed by the case of Li-compensated Al-associated centers in quartz. Even though detailed single-crystal EPR data exists on $[AlO_4/Li^+]^+$ (Nuttal and Weil, 1981; Howarth et al., 1997) and $[AlO_4/Li]^q$ (Walsby et al., 2003) we lack a structural model for the $[AlO_4/Li]^q$ defect center and a clear understanding of the formation mechanism for the two types of Li-compensated defect centers in quartz.

The lack of experimental techniques with comparable sensitivity to complement the EPR spectroscopy findings imposes an additional limitation to the study of defect centers in geologic samples. The incorporation of H in stishovite, in particular Al bearing stishovite is another example in which the complexity of the geologic system (i.e. high-pressure SiO_2 phase) and the relatively limited number of suitable experimental approaches (i.e. IR, FTIR, NMR), confer to the problem a high degree of difficulty.

1.2 Research Objectives and Rationale

In this context, computational modeling represents an excellent complementary way of exploring the structural and electronic properties of defects centers, offering new insight at the atomic level. Depending on the type of calculations, level of accuracy required and actual quantity to be calculated, one can choose between several computational procedures. In the case of defect center calculations (i.e. electronic properties, structural properties, magnetic properties) quantum mechanical calculations have proven to be the most accurate and reliable approach. In particular, density functional theory (DFT) is by far the most commonly used technique (Wright, 2006).

There are two basic computational strategies used for the study of point defects in solids, namely the cluster approach and the supercell method. When using the cluster method, only a finite number of atoms representing a fragment of the solid are considered explicitly, and usually the positions of the terminating atoms are kept fixed (Pachioni et al., 1992). The main advantage of this approach is its ability to investigate complex system such as defects in disordered solids, due to the absence of translational symmetry. Although the cluster approach has its advantages, its use in quantum mechanical calculations can be problematic due to the edge effects (i.e. nonphysical electronic states localised at the boundaries, levels in the band gap, neglect of Coulomb and exchange interactions with the environment) and the limited number of atoms that can be included in the cluster (Dovesi et al., 2005).

A more complex strategy, derived from the cluster method is the embedded cluster approach, which considers a quantum region or cluster embedded in a classical

one. In this way it smoothly links the quantum mechanical solution of the cluster to the perfect crystal.

Contrary to the cluster-based techniques, the supercell approach makes extensive use of the symmetry of the system. In this case the defect is enclosed in a supercell of a certain size and periodically repeated through the space. The advantage of this approach is that it provides a more realistic model of the crystalline system and makes use of its periodicity and quasi-periodicity. The disadvantage, however, results from the relatively high concentration of defects introduced in the system as a result of the limited size (i.e. tens to hundreds of atoms) of the supercell imposed by the computational resources.

However, despite the limitations, the easy implementation in all periodic *ab-initio* codes makes the supercell approach the method of choice in solid state physics and a widely use technique for the study of defect centers in crystalline systems (Dovesi et al., 2005; Wright, 2006).

For the purpose of the present research, *ab-initio* density functional theory calculations within the supercell approach were carried out using the CRYSTAL06 computer code. This particular code was chosen for its ability to use Hartree-Fock (HF), DFT and hybrid HF-DFT methodologies, with a large range of functionals. The code can investigate systems of any periodicity ranging from 0D to 3D with rigorous exploitation of symmetry (Dovesi et al., 2006).

Aiming to bring new, complementary data to the current understanding of defect structures in minerals, this body of research is focused on *ab-initio* quantum mechanical calculations of electron and hole centers in crystalline systems of geologic importance,

namely fluorite, quartz and stishovite. The thesis is divided into 4 parts, each a separate article for peer-reviewed publications.

Chapter 2 presents and discusses *ab-initio* calculations performed on the [O_2^{3-}-Y^{3+}] center in CaF_2 and SrF_2. The study is focused on the electronic and magnetic properties of [O_2^{3-}-Y^{3+}] and is intended to address and eliminate some of the controversies surrounding the existence of O_2^{3-}-type enters. The extensive experimental characterization (i.e. EPR and ENDOR data; Bill, 1969) that exist in the literature on [O_2^{3-}-Y^{3+}] in CaF_2 and SrF_2, made these crystalline systems ideal for the purpose of this research. Mr. Davy Adriaen (PhD student at University of College of London) assisted me in implementing the CRYSTAL06 code during the initial stage of this study and was included as a co-author of a paper which stemmed from this chapter.

The structural properties of [AlO_4/M^+] defects in quartz are the second topic addressed by the present research. Quantum mechanical calculations of both diamagnetic and paramagnetic [AlO_4/M^+] defects in quartz are presented in Chapter 3 and Chapter 4, respectively, with the purpose to provide a more complete picture for the Al^{3+}-M^+ coupled substitutions and better constrain the structural models derived from the experimental studies. The implications for the uptake of Al in quartz are also considered.

The coupled Al-M^+ substitution is further investigated in stishovite, the high-pressure polymorph of SiO_2. The structure, the electronic and magnetic properties of the experimentally reported [O_2^{3-}-Al^{3+}] defect (Ogoh et al., 1996) is investigated at the DFT level. Possible precursors of this paramagnetic center are considered and the significance of the incorporation of light elements (i.e. H, Li and Na) charge compensators is discussed in detailed in Chapter 5.

2.4 References

Bell DR, Rossman GR (1992) Water in earth mantle: The role of nominally anhydrous minerals, Science, 255:1391-1397

Bill H (1969) Investigation on colour centres in alcaline earth fluorides. Helvetic Physica Acta 42: 771-797

Botis SM, Nokhrin S, Pan Y, Xu Y, Bonli T, Sopuck V (2005) Natural radiation-induced damage in quartz. I. Correlations between cathodoluminescence colors and paramagnetic defects. Canadian Mineralogist 43: 1565-1680

Botis SM, Pan Y, Nokhrin S, Nilges M (2008), Natural radiation-induced damage in quartz.III. A new ozonide radical in drussy quartz from the Athabasca Basin, Saskatchewan. Canadian Mineralogist 46: 125-138

Che M, Tench AJ (1983) Characterization and reactivity of molecular oxygen species on oxide surfaces. Advances in Catalysis 32: 1-148

Dovesi R, Civalleri B, Orlando R, Roetti C, Saunders V (2005) Ab initio simulations in solid state chemistry, vol. 21, Wiley-VCH, John Wiley & Sons, Inc.

Dovesi R, Saunders VR, Roetti C, Orlando R, Zicovich-Wilson CM, Pascale F Civalleri B, Doll K, Harrison NM, Bush IJ, D'Arco P, Llunnell M (2006) CRYSTAL2006, User's Manual; http://www.crystal.unito.it, University of Torino, Torino

Howarth DF, Mombourquette MJ and Weil JA (1997) The magnetic properties of the oxygen-hole aluminum centers in crystalline SiO_2. V. ^{17}O-enriched $[AlO_4/Li]^+$ and dynamics thereof. Canadian Journal of Physics, 75: 99-115

Ikeya M (1993) New applications of electron paramagnetic resonance: ESR dating, dosimetry, and spectroscopy. World Scientific, Singapore

Ingrin J, Skogby H (2000) Hydrogen and nominally anhydrous upper-mantle minerals minerals: concentration levels and implications. European Journal of Mineralogy, 12: 543-570

Marfunin AS (1995) Composition, structure and properties of mineral matter. Springer, Berlin

Murphy DM, Chiesa M (2004) EPR of paramagnetic centres on solid surfaces. Electronic Paramagnetic Resonance, 19: 279-317

Nilges MJ, Pan Y, Mashkovtsev RI (2008) Radiation-damage-induced defects in quartz. I. Single-crystal W-band EPR study of hole-centers in an electron-irradiated quartz. Physics and Chemistry of Minerals 32: 103-115

Nuttall RHJ and Weil JA (1981) The magnetic properties of the oxygen-hole aluminum centers in crystalline SiO_2. II. $[AlO_4/H^+]^+$ and $[AlO_4/Li^+]^+$, Canadian Journal of Physics, 59: 1709-1718

Ogoh K, Yamanaka C, Ikeya M, Ito E (1996) Two center model for radiation induced aluminum hole center in stishovite. Journal of Physics and Chemistry of Solids 57: 85-88

Pacchioni G, Bagus PS, Parmigiani F (Eds) (1992) Cluster models for surface and bulk phenomena. vol 283, Plenum Press, New York

Pan Y, Botis S, Nokhrin S (2006) Application of natural radiation-induced paramagnetic defects in quartz to exploration in sedimentary basins. Journal China U Geosciences, 17: 258-271

Petroff S (1950) Photochemical observation of KCl crystals, Z Physick 127: 443-454

Regenauer-Lieb K, Hobbs B, Yuen DA, Ord A, Zhang Y, Mulhaus HB, Morra G (2006) From point defects to plate tectonic faults, Philosophical Magazine, 86: 3373-3392

Requardt A, Lehmann G (1985) An O23- radiation defect in A1PO4 and GaPO4. Journal of Physics and Chemistry of Solids, 46: 107-112

Rink WJ (1997) Electron spin resonance (ESR) dating and ESR applications in Quaternary Science and Archaeometry. Radiation Measurements, 27, 5: 975-1025

Rossman GR (1994) Colored varieties of silica minerals. Reviews in Mineralogy, 29: 433-467

Seidel H (1961) Elektronen-kern-doppelresonanz-soektren von F-zentren in alkalihalogenoid-kristallen. Z Physick 165, 2: 218-238

Teal GK, Little JB (1950) Growth of germanium single crystals, Physical Review 78: 647-647

Tilley RJD (1987) Defect crystal chemistry and its applications. Chapman and Hall, NY.

Walsby CJ, Less NS, Claridge RFC, Weil JA (2003) The magnetic properties of oxygen-hole aluminum centers in crystalline SiO_2. VI. A stable AlO_4/Li center. Canadian Journal of Physics, 81: 583-597

Weil JA, Wertz J, Bolton J (1994) Electron paramagnetic resonance: Elementary theory and practical application. John Wiley & Sons, New York, NY, USA

Wright K (2006) Atomistic models of OH defects in nominally anhydrous minerals, In Keppler H, Smyth JR (Eds), Water in nominally anhydrous minerals, Reviews in Mineralogy and Geochemistry, 62: 67-83

Chapter 2

Ab- initio calculations on the [O_2^{3-}-Y^{3+}] center in CaF_2 and SrF_2

The O_2^{3-}-Y^{3+} center in fluorite-type structures (CaF_2 and SrF_2) has been investigated at the density functional theory (DFT) level using the CRYSTAL06 code. Our calculations were performed by means of the hybrid B3PW method in which the Hartree-Fock exchange is mixed with the DFT exchange functional, using Becke's three parameter method, combined with the non-local correlation functionals by Perdew and Wang. Our calculations confirm the stability and the molecular character of the O_2^{3-}-Y^{3+} center. The unpaired electron is shown to be almost exclusively localized on and equally distributed between the two oxygen atoms that are separated by a bond distance of 2.47Å in CaF_2 and 2.57 Å in SrF_2. The calculated ^{17}O and ^{19}F hyperfine constants for of the O_2^{3-}-Y^{3+} center are in good agreement with their corresponding experimental values reported by previous electron paramagnetic resonance (EPR) and electron nuclear double resonance (ENDOR) studies, while discrepancies are notable for the ^{89}Y hyperfine constants and are probably attributable to an inadequate basis set for Y.

2.1 Introduction

Charged molecular oxygen species, including O_2^+, O_2^-, O_3^-, O_2^{2-} and O_2^{3-}, occur as structural imperfections and defects both in bulk and on the surfaces of various compounds and have long attracted extensive studies owing to their important roles in a wide range of materials (e.g., catalysts, minerals, semiconductors, nano-particles and bio-films; Lunsford, 1973, Marfunin, 1979; Che and Tench, 1983, Murphy and Chiesa, 2004). With the exception of O_2^{2-} all species are paramagnetic and therefore are amenable to detailed studies by electron paramagnetic resonance (EPR) spectroscopy. As a result, extensive data exist for the O_2^+, O_2^- and O_3^- species in the literature (Che and Tench, 1983; Murphy and Chiesa, 2004). However, only limited EPR studies are available for O_2^{3-}, even in crystalline solids (Nilges et al., 2008), and questions remain about its bond distance and whether O_2^{3-} is a true molecular ion or a hole is rapidly exchanged between two oxygen atoms (Requardt and Lehmann, 1985). Moreover, the identification of the O_2^{3-} centers by use of EPR techniques is problematic owing to the great similarity between O_2^- and O_2^{3-} structural models (e.g., O_2^--Al^{3+} vs. O_2^{3-}-Al^{3+}, Nilges et al., 2008).

This aspect is particularly important for minerals like fluorides and quartz, in which several charged molecular oxygen species, including O_2^{3-}, have been reported as characteristic radiation-induced defects (Bill, 1969; Nilges et al., 2008). These defects are important color centers (Bill, 1969; Marfunin, 1979; Botis et al., 2005) and have applications as natural dosimeters and geochronometers to a wide range of areas from anthropology to archaeology, nuclear waste disposal and mineral exploration (Ikeya, 1993; Pan et al., 2006). Therefore, a better understanding of the stabilities and the electronic structure of the O_2^{3-} type centers is of crucial importance and could clarify the

overly complicated picture of magnetically similar molecular oxygen species in various materials.

A free O_2^{3-} ion with 19 electrons, isoelectronic with the F_2^- center, is expected to have the unpaired electron in an antibonding orbital ($p\sigma^*$). Jette et al. (1969), on the basis of theoretical calculations, showed that the F_2^- center is a stable molecular ion and reported its internuclear distance to be matrix dependent, ranging from 1.905 Å for a free ion to 2.11 Å in LiF and 2.19 Å in both KF and RbF. Similarly, density functional theory (DFT) calculations by Nilges et al. (2008) showed that the free F_2^- ion forms a bond at 2.016 Å, whereas O_2^{3-} does not form a bond. Nilges et al. (2008) attributed the instability of O_2^{3-} over F_2^- to a 25% reduction in the attractive nucleus-electron energy.

While questions remain about the existence of an isolated O_2^{3-} ion, it is possible that O_2^{3-} can be stabilized by complexation, particularly with transition metals. For example, O_2^{3-}–M^{3+} centers (where M = Y, Al…) have been suggested to occur in several compounds (Bill, 1969; Bershov et al., 1971; Wagner and Murphy, 1972; Lagendij et al., 1973; Solntsev et al., 1973; Requardt and Lehmann, 1985; Ogoh et al., 1996; Schweizer and Spaeth, 1999). Of these, the O_2^{3-}-Y^{3+} center in synthetic CaF_2 and SrF_2 is the best-studied example, for which ^{17}O, ^{19}F and ^{89}Y hyperfine constants are available (Bill, 1969). Accordingly, this contribution reports on a periodic *ab initio* calculation on the O_2^{3-}-Y^{3+} center in CaF_2 and SrF_2 to determine its stability, geometry, electronic structure and magnetic properties with particular attention to the hyperfine coupling tensors between the unpaired electron and the neighboring nuclei.

2.2 Review on experimental results

Bill (1969) reported a detailed EPR and electron nuclear double resonance (ENDOR) study of two oxygen hole centers in X-ray irradiated, Y-doped CaF_2 and SrF_2, and interpreted one of them to represent an O_2^{3-}-Y^{3+} complex. Bill (1969) proposed this complex in CaF_2 to originate from an Y^{3+} ion and two O^{2-} ions substituting for a Ca^{2+} ion and two neighboring F^- ions and hole trapping by the two oxygen ions during X-ray irradiation. The O_2^{3-}-Y^{3+} complex has been shown to have a C_{2v} symmetry with 12 possible orientations in the Fm3m fluorite structure (Fig. 2.1), six of them being magnetically nonequivalent. Spin-Hamiltonian parameters for this complex from the EPR experiments included hyperfine constants involving one ^{89}Y (I=1/2), two ^{19}F (I=1/2) and one ^{17}O (I=5/2). Moreover, in the case of CaF_2, ENDOR measurements allowed determination of the hyperfine interactions between the unpaired electron and the first seven F neighbors, but the signs of these hyperfine tensors remain uncertain (Bill 1969).

Bill (1969) noted that the hyperfine constants of ^{17}O and ^{89}Y of this center in CaF_2 and SrF_2 are almost independent of the lattice parameters and concluded that the O_2^{3-}-Y^{3+} center has a strong molecular character. Bill (1969) also observed that the ^{19}F hyperfine structures strongly depend on the lattice parameters, indicative of lattice ions. However, Bill (1969) was unable to determine the presence or absence of a Ca^{2+} cation on the other side of the O_2^{3-} molecule ion: i.e., whether the complex is actually $(CaYO_2)^{2+}$ or (YO_2).

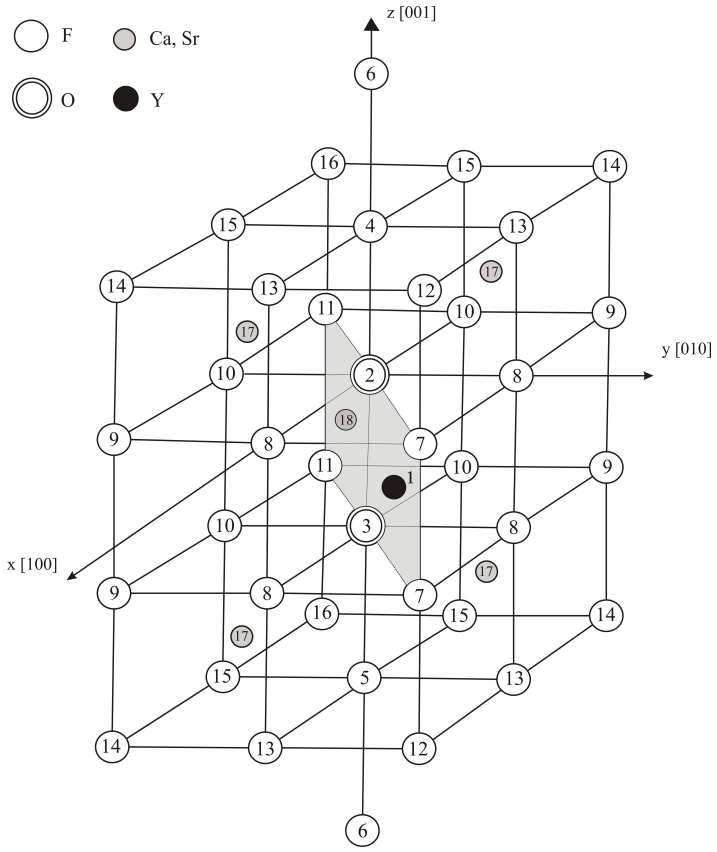

Figure 2.1: Ideal fluorite-type structure (CaF_2 and SrF_2) with an (O_2^{3-} -Y^{3+}) defect center incorporated (modified from Bill, 1969). Note that the symmetrically equivalent atoms are labeled with the same number. Also, the plane including the Y atom and the two O atoms is shaded.

2.3 Computational details

All calculations were performed with the CRYSTAL06 code, which computes the electronic structures and properties of periodic systems by use of the Hartree-Fock (HF), DFT and various hybrid approximations (Dovesi et al., 2006). CRYSTAL06 employs Gaussian-type functions (GTF) localized at atoms as the basis set for an expansion of the crystalline orbitals. The code can solve HF and Kohn-Sham equations with local, non-local and hybrid potentials.

The basis sets include those of Ca and F from Catti et al. (1991), O from Valenzano et al. (2006), the full-electron (26s17p10d) → [5s4p3d] contracted set for Y developed by Towler (1995). In the case of Sr, the basis set was a Hay-Wadt effective core potential (Hay and Wadt, 1985a,b) with a valence basis consisting of 311(1d) contractions of GTFs, developed by Piskunov et al., 2004. The exchange-correlation contribution is the result of a numerical integration of the electron density and its gradient performed over a grid of points. In order to obtain high accuracy energy calculation and geometry optimization, a pruned grid consisting of 75 radial points and 974 angular points was used (XLGRID). The high accuracy grid is recommended for calculations involving heavy atoms (fourth row and heavier) (Dovesi et al., 2006).

The reciprocal space integration was performed by sampling the Brillouin zone of the unit cell with the 8*8*8 Pack-Monkhorst net (for calculations of the bulk structure) and a 4*4*4 Pack-Monkhorst net (for calculations employing a 48-atom supercell) (Monkhorst and Pack, 1976).

CRYSTAL has standard values for its treatment of Coulomb and Exchange integrals, based on an assumed s-orbital-like overlap coefficient. We used the standard CRYSTAL values (6, 6, 6, 6, 12) for the integrals. This means that the overlap between two basis functions was disregarded when the overlap was less than 10^{-6} AU, and that the second-degree overlap was ignored when this was $< 10^{-12}$ AU (Dovesi et al., 2006).

The convergence criteria for the self-consistent field (SCF) energy and eigenvalues were the standard values between 10^{-6} and 10^{-5}, while the tolerance in change of total energy between optimization steps was set to 10^{-7} hartree.

The supercell model was used for the calculation of the (O_2^{3-}-Y^{3+}) center. A major problem for the application of the supercell model is the possibility of interaction between defects in the neighboring supercells. Therefore, the size of the supercell must be so chosen to maximize the distance between adjacent point defects and reduce the degree of their interaction. On the basis of detailed results of Shi et al. (2005) regarding the effect of the supercells on various defect properties in the case of the F center in CaF_2, we adopt a supercell of 48 atoms for the present study.

2.4 Results and discussion

2.4.1 CaF_2 and SrF_2 bulk electronic structures

The bulk electronic structure of CaF_2 has been investigated by several previous *ab- initio* calculations (Dyke and Wright, 1990; Salzner and Schleyer, 1990; Lichanot et al., 1995; Catti et al., 2004; Merawa et al., 2003, Verstraete and Gonze, 2003; Shi et al., 2005). It is well known that the HF approach considerably overestimates the band gap of optical materials. On the other hand, 'pure' DFT methods like generalized gradient approximations (GGA) and meta-GGA's underestimate it (Pisani, 1996; Mijalko et al., 2004). In this context a hybrid exchange-correlation functional becomes the method of choice. In the present study, we have tested four functionals: PW91 exchange (Perdew and Wang, 1986; 1989; 1992; Perdew 1991) and correlation GGA, PBE exchange and correlation (Perdew et al.1996), B3PW (using Becke's three parameter exchange functional and Perdew and Wang's correlation functional), and the B3LYP method that employs Becke's exchange functional (Becke, 1993; 1996) and Lee, Yang and Parr's correlation functional (Lee et al., 1988). Similar to the results reported by Shi et al.

(2005), the hybrid B3PW method gives the best agreement between experimentally determined and calculated lattice parameters (i.e., overestimating the lattice parameter by only 0.53% in the case of CaF_2 and by 0.51% in the case of SrF_2; Table 2.1). Therefore, the B3PW functional was selected for all calculations of the (O_2^{3-}-Y^{3+}) center in CaF_2 and SrF_2.

Table 2.1: Comparison of calculated and experimental lattice parameters and band gaps for CaF_2 and SrF_2.

	Lattice constant (Å)	Error Δ (%)	Band gap (eV)	Error Δ (%)
CaF_2				
Experimental	5.46[a]		11.8[b]	
PWGGA	5.50	+0.86	8.68	-26.44
PBE	5.18	-5.10	8.67	-26.52
B3PW	5.48	+0.53	10.88	-7.79
B3LYP	5.51	+0.95	10.76	-8.81
SrF_2				
Experimental	5.80[c]		10.8[b]	
PWGGA	5.85	+0.86	8.84	-18.14
PBE	5.86	+1.03	9.01	-16.57
B3PW	5.83	+0.51	10.96	+1.48
B3LYP	5.86	+1.03	11.39	+5.46

References a, b, and c are Nicolov (2000), Frandon et al. (1972) and Wyckoff (1963), respectively.

2.4.2 Geometry and electronic structure of the (O_2^{3-}-Y^{3+}) center

The (O_2^{3-}-Y^{3+}) defect center was added to the supercell following the structural model proposed by Bill (1969). Two adjacent fluorine atoms were replaced by two oxygen atoms, and simultaneously a calcium atom was replaced by an yttrium atom (Fig.

2.1). After the introduction of the defect in the supercell, the atomic configuration of the surrounding atoms was allowed to relax using a minimization of the total energy as a function of the atomic displacements from the regular lattice sites.

The relaxation of the atoms surrounding the Y atom is relatively small (Table 2.2) for both structures.

Table 2.2: Bond distance and bond population of the (O_2^{3-}-Y^{3+}) center

System	r_i (Å)	r_j (Å)	Δr (Å)	B(i-j) (e)
CaF_2				
Y-O2	2.376	2.162	0.214	0.050
Y-O3	2.376	2.163	0.213	0.043
Y-F8	2.376	2.336	0.040	0.032
Y-F7	2.376	2.389	-0.012	0.024
O2-O3	2.745	2.470	0.275	0.012
Ca18-O2	2.376	2.353	0.023	0.001
Ca18-O3	2.376	2.354	0.022	0.001
SrF_2				
Y-O2	2.561	2.210	0.351	0.081
Y-O3	2.561	2.215	0.346	0.080
Y-F8	2.561	2.464	0.097	0.015
Y-F7	2.561	2.471	0.090	0.014
O2-O3	2.957	2.579	0.366	0.034
Sr18-O2	2.561	2.592	-0.031	-0.034
Sr18-O3	2.561	2.595	-0.034	-0.033

r_i and r_f represent the initial and relaxed bond distances, respectively.

Δr is the difference between the initial and the final (relaxed) bond distances. B(i-j) is the bond population. Labels of atoms are same as those in Figure 2.1.

However, starting from the perfect lattice geometry the two substitutional O atoms are moving towards each other; the internuclear distance being reduced by 10% in CaF_2 and 12.8% in SrF_2. Also, there is very limited relaxation between Ca_{18} and the two oxygen atoms (~1%, Table 2.2; Fig. 2.1). Therefore, Ca_{18} resides at a regular lattice site and does not play any significant role in stabilizing the O_2^{3-} defect, hence a $(YO_2)^0$ complex exists (Bill, 1969). Similarly, Sr_{18} does not appear to relax significantly away from its regular lattice site either.

Information regarding the overlap population and thus the bond characteristics is provided in the B(i-j) column of Table 2.2. The overlap population is useful in evaluating the covalent, ionic or metallic nature of bonds in a compound. For fully ionic compounds, B(i-j) ranges from negative values, describing the repulsive interaction between the electrons of cations and anions, to values in the very close vicinity zero. A high positive bond population indicates a high degree of covalency in the bond (Segall et al., 1996).

The Ca-F and Sr-F bond populations in bulk CaF_2 and SrF_2 are 0.003 and -0.022, respectively. The values of the overlap population obtained for (O_2^{3-}-Y^{3+}) center are situated in between the values generally reported for ionic bonds and the values reported for covalent bonds. The increased values of the bond population for the (O_2^{3-}-Y^{3+}) center (Table 2.2) are due to the important participation of the d orbitals of Y and the p orbitals of O.

The charge density maps (Fig. 2.2 a, c) illustrate the molecular character of the (O_2^{3-}-Y^{3+}) center. An analysis of the effective charges of atoms surrounding the defect center (Table 2.3) along with the analysis of the spin density maps (Fig. 2.2 b, d) shows

that the unpaired spin is localized almost exclusively on the two oxygen atoms and is equally distributed between them.

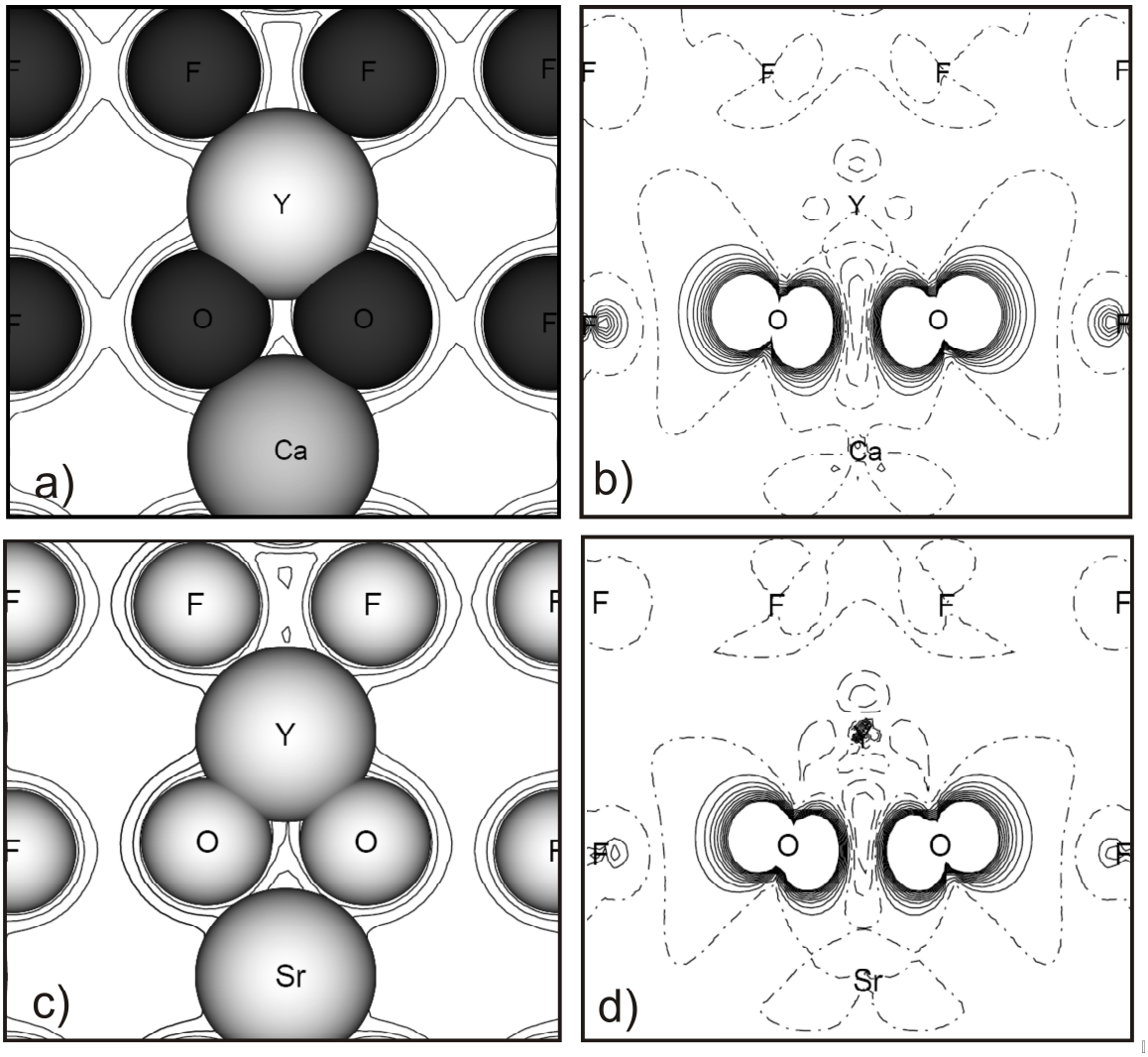

Figure 2.2: Electron charge density maps at the valence band maximum (a and c; cf. Carrier and Wei 2004) and the spin charge density maps (b and d) of the (O_2^{3-}-Y^{3+}) center in CaF_2 and SrF_2. The separation between the isodensity curves is 0.01 *e*/bohr^3. Continuous, dashed and dot-dashed lines denote positive, negative and zero values respectively.

The formation of the (O_2^{3-}-Y^{3+}) center in CaF_2 can be written:

$$2Ca_xF_{2x}+Y_2O_3+1/2*O_{2(g)} \rightarrow 2Ca_{x-1}F_{2x-2}YO_2+2CaF_2$$

Therefore, its formation energy can be calculated using the following expression:

$$E^{formation} = 2*E(Ca_{x-1}F_{2x-2}YO_2)+2*E(CaF_2)-1/2*E(O_{2(g)})-E(Y_2O_3)-2*E(Ca_xF_{2x})$$

where x is dependent on the size of the supercell employed for calculation (i.e., 16 for the 48-atom supercell). The analogous formula can be used for the calculation of the formation energy of the defect in SrF_2. The calculated formation energies for the (O_2^{3-}-Y^{3+}) center in CaF_2 and SrF_2 are 4.04 eV and 6.43 eV, respectively, same order of magnitude to the formation energy of the F center in CaF_2 (7.87 eV, cf. Shi et al. 2005).

Table 2.3: Effective charges and relative displacements of the (O_2^{3-}-Y^{3+}) center and its neighboring atoms

	Atom displacement			Spin population
	Δx (Å)	Δy (Å)	Δz (Å)	(n_α-n_β) (*e*)
CaF_2				
Y	-0.0722	0.0756	-0.0007	-0.043
O2	0.0094	-0.0786	0.1371	0.513
O3	0.0065	-0.0813	-0.1374	0.514
F8	-0.0257	-0.0450	0.0052	-0.001
F7	0.0266	-0.0584	0.0248	0.005
Ca18	0	0	0	0.001
SrF_2				
Y	0.0861	0.1053	-0.0016	-0.061
O2	-0.1010	-0.1230	-0.1924	0.524
O3	-0.1024	-0.1215	0.1861	0.531
F8	0.0351	-0.0727	-0.0506	0.002
F7	-0.0630	-0.0064	-0.0573	0.002
Sr18	0	0	0	0.000

Labels of atoms are the same as those in Figure 2.1.

2.4.3 Hyperfine coupling constants

Due to the presence of an unpaired electron and the interaction between the unpaired spin and the spin of the neighboring nuclei, a hyperfine structure of the EPR spectra can be detected. The hyperfine interaction tensor includes both isotropic and anisotropic components. The isotropic hyperfine interaction *a,* is caused by the non-zero probability of an electron being in the position of a given nucleus.

$$a = \frac{2\mu_0}{3h} g\beta_e g_N \beta_n \rho^{\alpha-\beta}(0) \tag{2.1}$$

In the expression of the isotropic component of the hyperfine interaction all the multiplicative factors are tabulated constants with the exception of the spin density $\rho^{\alpha-\beta}$ at N, which is the only term that depends on the electronic structure of the system. In the present calculations the g factor is approximated as being equal to the electronic g factor (2.0023), which is usually an acceptable approximation (Mallia et al. 2001).

The anisotropic contribution *b* is due to the presence of higher order poles and it is indicative of the deformation of the electronic density with respect to the spherical contribution.

$$b = \frac{\mu_0}{4\pi h} g\beta_e g_N \beta_n \left[T_{11} - \frac{1}{2}(T_{22} + T_{33}) \right] \tag{2.2}$$

T is a tensor of rank 2, which is obtained as the field gradient of the spin density at N and its generic element has the form:

$$T_{ij}^N = \sum_{\mu\nu} \sum_G P_{\mu\nu G}^{\alpha-\beta} \int \varphi_\mu(r) \left(\frac{r^2 \delta_{ij} - 3 r_i r_j}{r^5} \right) \varphi_\nu(r - G) dr \tag{2.3}$$

where the origin of the Cartesian system is at the nucleus (*N*), $\varphi_\nu(r\text{-}G)$ is the νth atomic orbital centered in the cell and $P_{\mu\nu G}^{\alpha-\beta}$ is the difference between the density matrices of electrons with α and β spin(i.e. a measure of the spin density). T_{ii} are the diagonal elements of the tensor, following the convention that T_{11} is the maximum module component (Mallia et al., 2001).

The crucial requirement for obtaining reliable results is therefore the availability of reliable spin densities at the nuclear position (see Eq. 2.1). In this context, the choice of the functional is very important and the performance of the different functionals is strictly related to their ability to provide good spin densities not on average but at these very positions. The best results were reported to be obtained using the hybrid schemes and large and flexible basis sets (Koch and Holthausen, 2000). The calculated principal values of the hyperfine tensor are in good agreement with the experimental values obtained from EPR and ENDOR measurements (Tables 2.4 and 2.5).

Table 2.4: Comparison of calculated and experimental hyperfine constants

	CaF_2		SrF_2		Nucleus
	Experimental (Gauss)	Calculated (Gauss)	Experimental (Gauss)	Calculated (Gauss)	
A_x	4.11±0.04	-2.68	4.08±0.08	-2.67	
A_y	3.96±0.04	-2.52	3.80±0.08	-2.75	^{89}Y
A_z	4.27±0.04	-2.60	4.19±0.08	-2.50	(I=1/2)
A_x	18.67±0.03	18.5	9±1.5	6.87	
A_y	5.20±0.03	4.49	≤ 2	1.45	^{19}F
A_z	4.95±0.03	4.08	≤ 2	1.45	(I=1/2)
A_x	72.7±1.1	-82.0	71.9±1.1	-82.33	
A_y	6±2.5	-2.01	5±2.5	-0.44	^{17}O
A_z	6±2.5	-1.82	5±2.5	-0.59	(I=5/2)

EPR and ENDOR experimental data from Bill (1969)

The only exception is the notable discrepancies between the experimental and calculated values of the ^{89}Y hyperfine constants (Tables 2.4 and 2.5), which are most likely attributable to Y's larger number of electrons and the size limitation of its basis set used (Towler 1995). Attempts to optimize the Y basis set of Towler (1995) have been made by allowing variation of the original exponents up to 60%, but no significant improvements in the calculated values of the ^{89}Y hyperfine constants for the O_2^{3-}-Y^{3+} center in CaF_2 were achieved.

Table 2.5: Comparison of calculated and ENDOR experimental data for the (O_2^{3-}-Y^{3+}) center in CaF_2

Nuclei	Experimental (Gauss)	Calculated (Gauss)
Y	± 4.114	-2.676
F4	±10.429	8.734
F5	±10.429	8.851
F6	± 0.124	0.206
F8	-1.479	-2.277
F10	-1.003	-1.492
F9	0.014	-0.013
F14	± 0.241	-0.211

ENDOR experimental data from Bill (1969).
Labels of atoms are the same as those in Figure 2.1.

2.5 Conclusions

These are the first ab initio calculations of the O_2^{3-} type defects in crystalline solids at the DFT level. Our results confirm the stability and the molecular character of the (O_2^{3-}-Y^{3+}) center in CaF_2 and SrF_2. In particular, the unpaired electron is shown to be almost exclusively localized on and equally distributed between the two oxygen atoms that are separated by a distance of 2.47 Å in CaF_2 and 2.57 Å in SrF_2. The calculated ^{19}F and ^{17}O hyperfine constants are in good agreement with experimental values, while considerable discrepancies are apparent between the calculated and experimental ^{89}Y hyperfine constants and point to the need for a larger or more flexible basis set for Y.

2.6 References

Bill H (1969) Investigation on colour centres in alcaline earth fluorides. Helvetic Physica Acta 42: 771-797

Botis SM, Nokhrin S, Pan Y, Xu Y, Bonli T, Sopuck V (2005) Natural radiation-induced damage in quartz. I. Correlations between cathodoluminescence colors and paramagnetic defects. Canadian Mineralogist 43: 1565-1680

Becke AD (1993) Density-functional thermochemistry. 3. The role of exact exchange. Journal of Chemical Physics 98: 648-5652

Becke AD (1996) Density-functional thermochemistry. 4. A new chemical correlation functional and implications for exact exchange mixing. Journal of Chemical Physics 104: 1040-1046

Bershov LV, Martiros VO, Marfunin AS, Speransk AV (1971) Yttrium-stabilised electron-hole centres in anhydrite. Physica Status Solidi B-Basic Research 44: 505-512

Catti M, Pavese A, Saunders VR (2004) Elastic constants and electronic structure of fluorite (CaF2): an ab initio Hartree-Fock study. Journal of Physics: Condensed Matter 3: 4151-4164

Catti M, Dovesi R, Pavese A, Saunders VR (1991) Elastic constants and electronic structure of fluorite (CaF2): an ab initio Hartree-Fock study. Journal of Physics: Condensed Matter 3: 4151-4164

Che M, Tench AJ (1983) Characterization and reactivity of molecular oxygen species on oxide surfaces. Advances in Catalysis 32: 1-148

Dyke JM, Wright TG (1990) An ab initio study of the equilibrium geometries and vibrational frequencies of the group-IIA difluorides BeF2, MgF2, CaF2. Chemical Physics Letters 78: 138-144

Dovesi R, Saunders VR, Roetti C, Orlando R, Zicovich-Wilson CM, Pascale F Civalleri B, Doll K, Harrison NM, Bush IJ, D'Arco P, Llunnell M (2006 CRYSTAL2006, User's Manual; http://www.crystal.unito.it, University of Torino, Torino

Hay PJ, Wadt WR (1985a) Ab initio effective core potentials for molecular calculations – potentials for the transition metal ions from Sc to Hg. Journal of Chemical Physics 82: 270-283

Hay PJ, Wadt WR (1985b) Ab initio effective core potential for molecular calculations-potentials for K to Au including the outermost core orbitals. Journal of Chemical Physics 82: 299-310

Hay PJ, Wadt WR (1985) Ab initio effective core potentials for molecular calculations – potentials for main group elements Na to Bi. Journal of Chemical Physics 82: 284-294

Ikeya M (1993) New applications of electron paramagnetic resonance: ESR dating, dosimetry, and spectroscopy. World Scientific, Singapore

Jette NA, Gilbert TL, Das TP (1969) Theory of self-trapped hole in alkali halides, Physics Review 184: 884-895

Koch W, Holthausen MC (2000) A chemist's guide to Density Functional Theory. Wiley-VCH, Weinheim

Lagendij A, Glasbeek M, Vanvoors JD (1973) Paramagnetic oxygen centers in SrTiO3 induced by light. Chemical Physics Letters 20: 92-95

Lee C, Yang W, Parr RG (1988) Development of the Colle-Salvetti correlation-energy formula into a functional of the electron density. Physics Review B 37: 785-789

Lichanot A, Rerat M, Catti M (1995) Theoretical ab initio calculations of the structure factors of fluorite (CaF2). Acta Crystallographica A 51: 323-328

Lunsford JH (1973) ESR of adsorbed oxygen species. Catalysis Review 8: 135-156

Mallia G, Orlando R, Roetti C, Ugliengo P, Dovesi R (2001) F center in LiF: A quantum mechanical ab initio investigation of the hyperfine interaction between the unpaired electron at the vacancy and its first seven neighbors. Physics Review B 63(23): 235102

Marfunin AS (1979) Spectroscopy, luminescence and radiation centers in minerals. Springer, Berlin

Mijalko EA, Dorsett HE, Ford MJ (2004) Trends in the band structures of the group-I and –II oxides. Journal of Chemical Physics 120: 10799-10806

Monkhorst HJ, Pack JD (1976) Special points for Brillouin-zone integrations. Physical Review B 13: 5188-5192

Merawa M, Llunell M, Orlando R, Geize-Duvignau M, Dovesi R (2003) Structural, electronic and elastic properties of some fluoride crystals: an ab initio study. Chemical Physics Letters 368: 7-11

Murphy DM, Chiesa M (2004) EPR of paramagnetic centres on solid surfaces. Electronic Paramagnetic Resonance 19: 279-317

Nicolov M. (2000) Shaped single crystals of CaF2. Journal of Crystal Growth, 218: 62-66

Nilges MJ, Pan Y, Mashkovtsev RI (2008) Radiation-damage-induced defects in quartz. I. Single-crystal W-band EPR study of hole-centers in an electron-irradiated quartz. Physics and Chemistry of Minerals 32: 103-115

Ogoh K, Yamanaka C, Ikeya M, Ito E (1996) Two-center model for radiation induced aluminum hole center in stishovite. Journal of Physics and Chemistry of Solids 57: 85-88

Pan Y, Botis S, Nokhrin S (2006) Application of natural radiation-induced paramagnetic defects in quartz to exploration in sedimentary basins. Journal China U Geosciences 17: 258-271

Perdew JP, Burke K, Ernzerhof M (1996) Generalized gradient approximation made simple. Physics Review Letters 77: 3865-3868

Perdew JP, Wang Y (1986) Accurate and simple density functional for the electronic exchange energy – generalized gradient approximation. Physics Review B 33: 8800-8802

Perdew JP, Wang Y (1989) Accurate and simple density functional for the electronic exchange energy: Generalized gradient approximation. Physics Review B 40: 3399-3399

Perdew JP, Wang Y (1992) Accurate and simple analytic representation of the electron-gas correlation-energy. Physics Review B 45: 13244-13249

Perdew JP (1991) Electronic structure of solids. Akademie Verlag Berlin

Pisani C (1996) Quantum mechanical ab-initio calculations of the properties of crystalline materials. Lecture Notes in Chemistry, 67, Springer, Berlin

Piskunov S, Heifets E, Eglitis RI, Borstel G (2004) Bulk properties and electronic structure of SrTiO3, BaTiO3, PbTiO3 perovskites: an ab initio HF/DFT study. Computational Matterial Science 29: 165-178

Requardt A, Lehmann G (1985) An O23- radiation defect in A1PO4 and GaPO4. Journal of Physics and Chemistry of Solids 46: 107-112

Salzner U, Schleyer PV (1990). An initio studies of the geometries and electronic structures of CaF2 and CaCl2. Chemical Physics Letter 172: 461-470

Schweizer S, Spaeth JM (1999) New oxygen hole centres in the x-ray storage phosphor BaFBr. Journal of Physics: Condensed Matter 11: 1723-1733

Shi H, Eglitis RI, Borstel G (2005) An initio calculations of the CaF2 bulk and F centers. Physics Review B, 72: 235102

Shi H, Eglitis RI, Borstel G (2007) Ab initio calculations of the oxygen-vacancy dipoles and M centers in CaF2. Computational Materials Science 39: 430-436

Segall MD, Shah R, Pickard CJ, Payne MC (1996) Population analysis of plane-wave electronic structure calculation of bulk materials. Physics Review B 54: 16317-16320

Solntsev VP, Shcherbakova MYa, Schastnev PV (1973) EPR study of structural defects in CaWO4. Zh Strukt Chim 14: 222-229

Towler M (1995) Crystal98 Resources Page. http://www.tcm.phy.cam.ac.uk/~mdt26/crystal.html

Valenzano L, Torres FJ, Doll K, Pascale F, Zicovich-Wilson CM, Dovesi R (2006) Ab Initio study of the vibrational spectrum and related properties of crystalline compounds; the case of CaCO3 calcite. Journal of Physical Chemistry 220: 893-912

Verstraete M, Gonze X (2003) First-principles calculations of the electronic, dielectric and dynamical properties of CaF2. Physics Review B 68: 195123

Wagner GR, Murphy J (1972) Paramagnetic hole centers in CeO2. Physics Review B 6: 1638-1644

Wyckoff RWG (1963) Crystal structures 1, 2nd ed., Interscience Publishers, New York

Chapter 3

Theoretical calculations of $[AlO_4/M^+]^0$ defects in quartz and implications for the uptake of Al

The $[AlO_4/M^+]^0$ (where M = H, Li, Na and K) defects in α-quartz have been investigated by *ab-initio* calculations at the density functional theory (DFT) level, using the CRYSTAL06 code, 72-atom supercells, and all-electron basis sets. The present DFT calculations yielded substantially improved results than previous cluster calculations with minimal basis sets. For example, the $[AlO_4/M^+(a_<)]^0$ defects with M = H, Li and Na have been shown to be more stable than their $[AlO_4/M^+(a_>)]^0$ structural analogues (where $a_>$ and $a_<$ denote the location of the charge compensating ion on the long-bond and short-bond side, respectively), correctly predicting the common occurrence of paramagnetic $[AlO_4/M^+(a_>)]^+$ centres. Also, the $[AlO_4/K^+]^0$ defects have been investigated for the first time and are shown to be stable in quartz. Moreover, our calculations confirm previous suggestions that incorporation of the $[AlO_4/M^+]^0$ defects results in significant structural relaxations that extend at least to the nearest Si atoms and give Li-O and Na-O bond distances in better agreement with the experimentally obtained values. The present theoretical results on the $[AlO_4/M^+]^0$ defects provide a more complete picture for the coupled Al^{3+}-M^+ substitutions, with implications for the uptake of Al in quartz.

3.1 Introduction

The structure of pure α-quartz (SiO_2; space group $P3_121$for left-handed crystals or $P3_221$ for right-handed ones) is composed of quasi-tetrahedral SiO_4 groups (Fig. 3.1; Le Page et al., 1980). The SiO_4 tetrahedra share corners to form spirals (or helices) along the crystallographic c-axis, resulting in two types of c-axis channels with different diameters (Fig. 3.1). The silicon atoms lie on alternate two-fold symmetry axes, whereas the oxygen atoms are in general positions. The site symmetry of silicon is 2 owing to the fact that there are two pairs of nonequivalent Si–O bonds (i.e., the short bonds at 1.610 and the long bonds at 1.614 at 94K; Le Page et al., 1980).

Aluminum is by far the most common trace element in virtually all varieties of natural quartz and is almost invariably present in their synthetic counterparts as well (Dennen et al. 1970; Weil, 1984). Aluminum and other impurity elements (e.g. H, Li, Na and K) in quartz are known to exert important influences on various physical and chemical properties of this common mineral and important material (e.g., stability, rheology, and diffusion; Kronenberg, 1994; Branlund and Hofmeister, 2007). Early interests in Al in quartz stemed largely from either its possible roles in the colors of this mineral (Griffiths et al., 1954; Cohen, 1956) or potential application as a geothermometer for constraining the formation conditions of host rocks (Dennen et al., 1970; Scotford, 1975; Götze et al., 2001). More recently, a resurgence of interest in Al and other trace elements in quartz comes as a result of 1) availability of microbeam techniques for high-precision, in-situ analysis and 2) recognition of their possible linkages to luminescence properties (e.g. Perny et al., 1992; Götze et al., 2001; 2005). For example, Al and other trace elements in quartz as determined by combined cathodoluminescence (CL) imaging

and in-situ analysis have become a petrogenetic tool for a wide range of applications from provenance of detritus to igneous and metamorphic processes, and fluid history in mineral deposits (e.g. Watt et al., 1997; Rusk et al., 2006; Müller et al., 2003, 2008).

Structural data on the incorporation of Al in quartz come almost exclusively from the technique of electron paramagnetic resonance (EPR) spectroscopy (e.g., Griffiths et al., 1954; Mackey 1963; Mackey et al., 1972; Nuttall and Weil, 1981a,b; Weil, 1984; Dickson and Weil, 1990; Howarth et al., 1997; Walsby et al., 2003; Nilges et al., 2008; Pan et al., 2008; Nilges et al., 2009). Griffiths et al. (1954) first discovered the possible presence of an $[AlO_4]^0$ centre in smoky quartz, which has since been confirmed both experimentally (Schnadt and Schneider, 1971; Nuttall and Weil, 1981a; Walsby et al., 2003) and theoretically (Pacchioni et al., 2001; To et al., 2005) and shown to represent a hole trapped on an oxygen atom linked to a substitutional AlO_4 tetrahedron by a long Al-O bond.

Mackey (1963) first detected the $[AlO_4/M^+]^+$ (where M=H, Li, Na) paramagnetic centres in quartz crystals that were irradiated and measured at 77K. Mackey (1963) noted that these centres lose the charge compensators on warming above 77K, giving rise to the $[AlO_4]^0$ centre. Subsequently, Mackey et al. (1970) published spin-Hamiltonian parameters for the $[AlO_4/H^+]^+$, $[AlO_4/Li^+]^+$, and $[AlO_4/Na^+]^+$ centres. In particular, Mackey et al. (1970) used the proton superhyperfine constant to locate the H^+ ion in the large c-axis channels, opposite to the oxygen atom on which the hole is trapped. Subsequently, Weil and co-workers determined the ^7Li and ^{23}Na superhyperfine parameters for the $[AlO_4/Li^+]^+$ and $[AlO_4/Na^+]^+$ centres (Nuttall and Weil, 1981b; Dickson and Weil, 1990) and the ^{17}O hyperfine parameters for the $[AlO_4/Li^+]^+$ centre

(Howarth et al., 1997). They too used the superhyperfine parameters to predict the locations of Li^+ and Na^+ ions in the large c-axis channels. Walsby et al. (2003) reported an $[AlO_4/Li]^q$ centre with an uncertain charge and an uncertain location of the Li compensator. The two suggested locations for Li were: 1) a site close to the centre of one of the two large c-axis channels and 2) a site on the edge of one of the small channels. Other Al-associated centres in quartz (e.g. Nilges et al., 2008; Pan et al., 2008; Nilges et al., 2009) have been shown to have substitutional Al ions located at tetrahedral sites as well.

Therefore, available EPR data for all Al-associated paramagnetic centres in quartz show that Al occurs exclusively at the tetrahedral sites and the $[AlO_4]^0$ associated centres most likely form from the $[AlO_4/M^+]^0$ precursors during irradiation (Mackey, 1963; Mackey et al., 1970; Weil, 2000). These $[AlO_4/M^+]^0$ precursors are diamagnetic and therefore cannot be investigated by the EPR technique. One question that arises is then how closely the $[AlO_4/M^+]^+$ paramagnetic centres reflect their respective diamagnetic precursors.

To answer this question, first-principles calculations have been made to evaluate the stabilities, geometries and the local structural environments of the $[AlO_4/M^+]^0$ defects in quartz (e.g. Mombourquette and Weil, 1985; Leslie, 1989; Cora and Pisani, 1994). However these previous studies, while having furnished important insights in interpreting the Al-associated defects, have several limitations: small clusters used, neglect of configuration interaction, neglect of the long-range polarization effects, and the use of minimal basis sets.

Accordingly, we have re-calculated the various $[AlO_4/M^+]^+$ paramagnetic centres (M = H, Li, Na and K) and their diamagnetic precursors at the density functional theory (DFT) level, using a supercell approach and all-electron basis sets. Our calculated results for the paramagnetic defects, including the various hyperfine and superhyperfine constants (^{27}Al, ^{17}O, ^{29}Si, ^{1}H, ^{7}Li and ^{23}Na), are in excellent agreement with experimentally determined values and allow a re-interpretation of the $[AlO_4/Li]^q$ center. In this contribution, we focus our attention on the stabilities, geometries and local structural environments of the diamagnetic precursors, including the $[AlO_4/K^+]^0$ defects for which paramagnetic derivatives have not been observed by EPR and no previous theoretical calculations have been made either. These results are used to provide new insights into the uptake of Al in quartz.

3.2 Computational methodology

All calculations have been performed with the CRYSTAL06 code, which computes the electronic structures and properties of periodic systems by use of the Hartree-Fock (HF), DFT and various hybrid approximations (Dovesi et al., 2006). CRYSTAL06 employs Gaussian-type functions (GTF) localized at atoms as the basis set for an expansion of the crystalline orbitals. The code can solve HF and Kohn-Sham equations with local, non-local and hybrid potentials.

Electron exchange and correlation effects were treated with the hybrid B3LYP functional, in which 20% of the HF exchange is mixed with 80% of DF exchange, combined with a non-local expression for the correlation proposed by Lee et al. (1988). The exchange-correlation contribution is the result of a numerical integration of the

electron density and its gradient performed over a grid of points. The sampling of the reciprocal unit cell was done with a 8*8*8 Pack-Monkhorst net (for calculations of the bulk structure) and a 4*4*4 Pack-Monkhorst net (for calculations employing a 72 atom supercells) (Monkhorst and Pack, 1976).

CRYSTAL has standard values for its treatment of Coulomb and exchange integrals, based on an assumed s-orbital-like overlap coefficient. We used the standard CRYSTAL values (6, 6, 6, 6, 12) for the integrals. This means that the overlap between two basis functions was disregarded when the overlap was less than 10^{-6} AU, and that the second-degree overlap was ignored when this was < 10^{-12} AU (Dovesi et al., 2006). The convergence criteria for the self-consistent field (SCF) energy and eigenvalues were the standard values between 10^{-6} and 10^{-5}, while the tolerance in change of total energy between optimization steps was set to 10^{-7} hartree.

The basis sets used for Si and O were those from Nada et al. (1990). The basis sets used for Al, H, Li, Na and K are those reported by Montanary et al. (2006), Dovesi et al. (1983), Merawa et al. (2004), Dovesi et al. (1991) and Civalleri et al (2003) respectively.

We have evaluated various sizes of supercells (up to 108 atoms) and noted that 72-atom supercells yield reasonable predictions for both the electronic structures and hyperfine/superhyperfine constants of the $[AlO_4/M^+]^+$ paramagnetic centres while the use of 108-atom supercells does lead to better agreement between calculated and experimental hyperfine/superhyperfine constants. The differences in the optimised geometries between the 72- and 108-atom supercells, however, are minimal.

Consequently, we adopted 72-atoms supercells for calculations of all diamagnetic defects in this study.

Calculations were first made to obtain the optimised geometry of pure α-quartz (Table 3.1). The various $[AlO_4/M^+]^0$ defects were then created by inserting an Al atom and an appropriate charge compensator into the optimised structure. The fact that each SiO_4 tetrahedron has two pairs of different Si-O bonds makes defects with the same charge compensator on different sides of the Si0 site nonequivalent (Fig. 3.1). In this study, we evaluated the two types of substitutions by keeping the charge compensator at the centre of supercells (i.e., the middle of a large c-axis channel) but changing the position of the substitutional Al atom from the Si0 site to the Si′ site across the c-axis channel (Fig. 3.1).

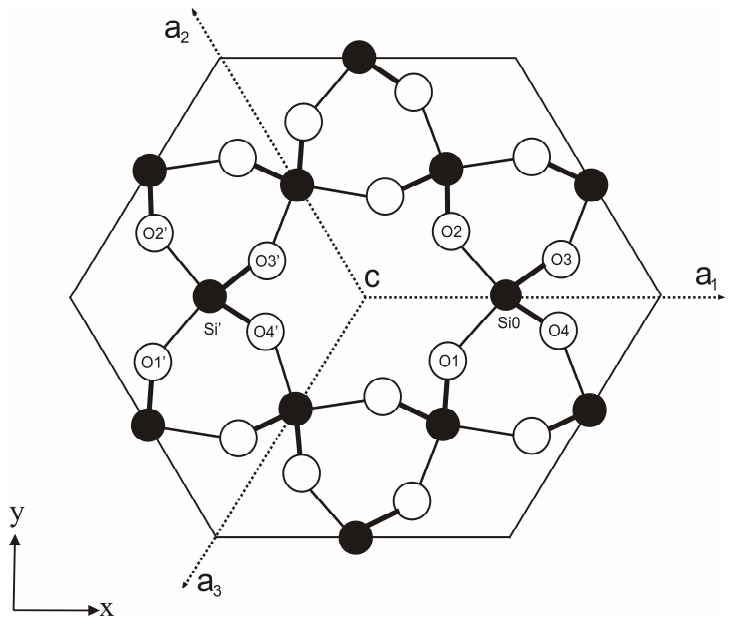

Figure 3.1: Structure of α-quartz ($P3_121$) projected on the (0001) plane (Le Page et al., 1980). The three two-fold axes a_1, a_2, and a_3 are indicated and the long Si-O bonds are marked by thick lines. Labels of Si0, O1, O2, O3 and O4 are same as in Mombourquette and Weil (1985). The four oxygen atoms around the Si' site are labeled as O1', O2', O3' and O4'.

This approach is equivalent to keeping the Al atom at the Si0 site but moving the charge compensator from one large c-axis channel to the other (Fig. 3.1; see Mombourquette and Weil, 1985). After the introduction of the $[AlO_4/M^+]^0$ defects in the supercell the structure was allowed to fully relax towards an energy minimum. The exception from this procedure was that only local relaxations (i.e., a fragment of 10 atoms) were allowed in the calculations of $[AlO_4/H^+]^0$, because insufficient hole localisation was obtained for the paramagnetic $[AlO_4/H^+]^+$ defects in the fully relaxed structures. Following Mombourquette and Weil (1985), we used the $a_<$ and $a_>$ symbols to indicate the location of the M^+ compensator with respect to the substituted Si atom (i.e. close to the short Si-O bond or the long Si-O bond, respectively).

3.3 Results

3.3.1 Structure of pure α-quartz

Numerous theoretical calculations have been made on pure α-quartz (e.g. Dovesi et al., 1987; Nada et al., 1990; Allan and Teter, 1990; Chelikowsky et al., 1990; Liu et al., 1994; Gnani et al., 2000). Our calculated lattice constants (a = 4.9336; c = 5.4439) for pure α-quartz are within 1% of the experimentally determined values (Le Page et al., 1980). The calculated fractional coordinates of Si and O atoms (Table 3.1) are also in good agreement with the experimentally determined values from single-crystal X-ray diffraction structure refinements measured at 94K (Le Page et al., 1980) and with previous theoretical calculations (e.g. Allan and Teter, 1990).

Table 3.1: Comparison of structural parameters of α-quartz

Parameter	LCG	This work	Error (%)	AP
a (Å)	4.9044	4.9332	0.58	4.8756
c (Å)	5.4010	5.4436	0.78	5.4052
Si (u)	0.46808	0.4646	-	0.4654
O (x)	0.41303	0.4106	-	0.4125
O (y)	0.27068	0.2770	-	0.2745
O (z)	0.11651	0.1112	-	0.1143

LCG are experimental data from Le Page et al. (1980).

AP are theoretical results from Allan and Teter (1990).

3.3.2 $[AlO_4/H^+]^0$ defects

Our calculations show that the $[AlO_4/H^+(a_<)]^0$ defect is 0.943 eV lower in the minimum energy than the $[AlO_4/H^+(a_>)]^0$ counterpart. Table 3.2 summarizes the calculated Cartesian coordinates of the Al, O and H atoms for the two types of $[AlO_4/H^+]^0$ defects. When comparing the relaxed structural environment of the defect with the ideal structure of pure α-quartz (Fig. 3.2), the largest relaxations in the $[AlO_4/H^+(a_>)]^0$ defect are the O1 and O3 atoms, while the largest displacements in the $[AlO_4/H^+(a_<)]^0$ involve the O1 and O2 atoms (note that the labels of oxygen atoms are those at the Si0 site). In both cases, Al is displaced from the a-axis, although to a smaller extent in the $[AlO_4/H^+(a_>)]^0$ defect. The calculated H-$O_<$ and H-$O_>$ bond distances are 0.983 Å and 0.985 Å, respectively.

The calculated angles between the O-H bond direction and the a-axis are 27.2° and 25.4° for the $[AlO_4/H(a_>)^+]^0$ and $[AlO_4/H(a_<)^+]^0$ defects, respectively. These angles are about 10º smaller that those deduced from the polarized IR spectra (Pankrath, 1991), which suggested two OH orientations with angles at ~36° and 34°. However, the

difference of about 2° between the two types of defects is consistent with that suggested by polarized IR spectra. Pankrath (1991) also noted that the angles from polarized IR are temperature dependent and therefore the ~10º difference may be attributable to difference in temperature (i.e., calculations for 0K versus IR measurements at 77K).

The calculated Al-O and H-O bond distances (Table 3.3) also show asymmetrical relaxation of the AlO_4 tetrahedron as well as a reduction in the local symmetry for both types of $[AlO_4/H^+]^0$ defects. For both structural models considered, the displacements of the nearest Si neighbors adjacent to the $[AlO_4/H^+]^0$ defects are as much as 0.11 Å, comparable to the magnitudes of displacement of the substitutional Al atom (Table 3.2; Fig. 3.2).

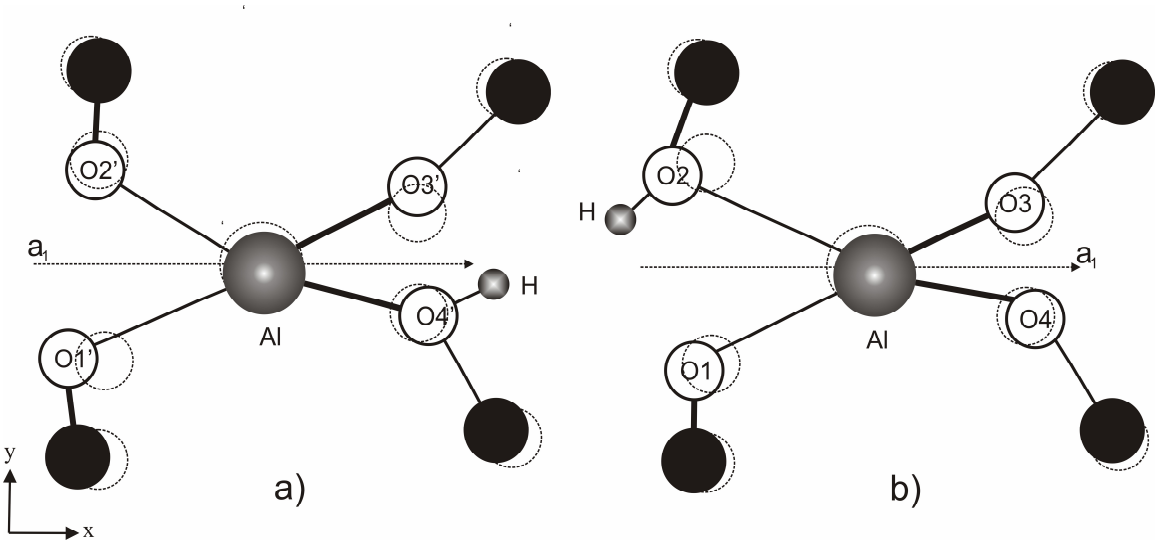

Figure 3.2: Structural models for a) $[AlO_4/H^+(a_>)]^0$ and b) $[AlO_4/H^+(a_<)]^0$, in comparison with the original Si and O positions of the ideal quartz structure (open circles). The original H position (not shown) was placed at the centre of the large c-axis channel (see text for explanation).

Table 3.2: Cartesian coordinates for the calculated $[AlO_4/M^+]^0$ defects

	Cartesian coordinates (Å)					
	x	y	z	x	y	z
$[AlO_4/H^+(a_>)]^0$				$[AlO_4/H^+(a_>)]^+$		
Al	2.1873	0.0178	0.1097	Al	2.2295	-0.1234	-0.0530
O1	1.3807	-1.3565	-0.6796	O1	1.2725	-1.1124	-0.7170
O2	1.2838	1.1439	0.5112	O2	1.5890	1.1822	0.6534
O3	3.5059	0.6197	-1.0793	O3	3.2259	0.7137	-1.2208
O4	3.2082	-0.5561	1.2846	O4	3.1193	-0.6431	1.2051
H	4.4957	-0.0046	-0.9712	H	4.4086	-0.1608	-0.8515
$[AlO_4/H^+(a_<)]^0$				$[AlO_4/H^+(a_<)]^+$		
Al	2.3364	-0.1342	0.0416	Al	2.3390	-0.0565	0.0119
O1’	1.2709	-1.2675	-0.5829	O1’	1.2711	-1.1691	-0.5604
O2’	1.1267	0.9910	0.4528	O2’	1.2046	1.1240	0.5395
O3’	3.1595	0.7043	-1.1018	O3’	3.2601	0.6392	-1.1202
O4’	3.2862	-0.6677	1.1148	O4’	3.2437	-0.6264	1.0880
H	0.4102	0.5482	-0.8643	H	0.4602	0.7647	-0.6884
$[AlO_4/Li^+(a_>)]^0$				$[AlO_4/Li^+(a_<)]^+$		
Al	2.1508	-0.0043	-0.0003	Al	2.3157	-0.1152	0.3719
O1	1.2278	-1.2220	-0.5624	O1	1.2866	-1.0642	0.1039
O2	1.2256	1.2134	0.5635	O2	1.3553	1.0776	0.3355
O3	3.3391	0.5399	-1.1003	O3	3.4245	0.1175	-0.6274
O4	3.3451	-0.5477	1.0930	O4	3.4128	-0.1277	1.1473
Li	4.8907	-0.0035	-0.0095	Li	5.0935	0.0273	0.2318
$[AlO_4/Li^+(a_<)]^0$				$[AlO_4/Li^+(a_<)]^+$		
Al	2.4580	0.0050	0.0041	Al	2.6513	-0.1084	0.1504
O1’	1.3007	-1.1105	-0.5887	O1’	1.5523	-0.9586	0.0117
O2’	1.3007	1.1201	0.5961	O2’	1.5654	0.9640	0.5123
O3’	3.3584	0.6354	-1.0715	O3’	3.6230	1.2131	-1.0169
O4’	3.3584	-0.6255	1.0797	O4’	3.6933	-1.1859	1.6249
Li	0.1814	0.0333	0.2841	Li	0.1019	0.0036	0.0020
$[AlO_4/Na^+(a_>)]^0$				$[AlO_4/Na^+(a_<)]^+$		
Al	2.0276	-0.0493	0.0215	Al	2.1870	0.1000	0.1600
O1	1.0912	-1.2098	-0.4545	O1	1.2759	-1.0776	0.2003
O2	1.1211	1.2193	0.6379	O2	1.1906	1.0648	0.4104
O3	2.9566	0.4116	-1.2416	O3	3.2224	0.0835	-0.6638
O4	3.3200	-0.5900	0.9911	O4	3.2457	-0.0933	1.1874
Na	4.9877	0.1208	-0.6109	Na	5.1012	-0.0453	0.2676
$[AlO_4/Na^+(a_<)]^0$				$[AlO_4/Na^+(a_<)]^+$		
Al	2.7142	-0.0201	-0.0184	Al	2.7877	-0.0908	0.1673
O1’	1.5723	-1.1390	-0.5822	O1’	1.7438	-0.9966	0.0518
O2’	1.6993	1.1853	0.5192	O2’	1.9217	0.5773	1.0674
O3’	3.5847	0.6307	-1.0701	O3’	3.6178	0.4619	-1.3126
O4’	3.6206	-0.6962	1.0787	O4’	3.7078	-0.0223	1.3413
Na	0.1269	0.2048	0.0832	Na	0.1808	0.0185	0.2910
$[AlO_4/K^+(a_>)]^0$				$[AlO_4/K^+(a_<)]^0$		
Al	1.8086	-0.1746	0.0702	Al	2.3176	0.8589	0.0181
O1	0.8503	-1.2768	-0.3446	O1’	1.3297	-0.3760	-0.5319
O2	1.0196	1.0750	0.4924	O2’	1.4420	1.9436	0.5509
O3	2.6915	0.0986	-1.1121	O3’	3.4171	1.3432	-1.0458
O4	2.9665	-0.5731	1.1158	O4’	3.0777	0.1477	1.0938
K	4.8396	0.3720	-0.7494	K	0.0267	0.2217	-0.0164

For each M^+ ion both types of possibilities at $a_<$ and $a_>$ have been evaluated. Also included for comparison are the coordinates of their paramagnetic derivatives.

Table 3.3: Calculated bond distances of the $[AlO_4/H^+]^0$ defects

	Bond distances (Å)			
	$[AlO_4/H(a_>)^+]^0$		$[AlO_4/H(a_>)^+]^+$	
	This study	MW	BP	MW
Al-O1'	1.704	1.707	1.656	1.646
Al-O2'	1.703	1.704	1.734	1.824
Al-O3'	1.713	1.717	1.704	1.659
Al-O4'	1.909	1.908	1.851	1.919
H-O1	2.102	-	2.833	-
H-O2	2.777	-	3.219	-
H-O3'	2.642	-	2.412	-
H-O4'	0.983	0.988	0.927	0.984
H-O*	2.908		3.193	
H-O*	2.550		3.613	
	$[AlO_4/H(a_<)^+]^0$		$[AlO_4/H(a_<)^+]^+$	
Al-O1	1.714	1.708	1.719	-
Al-O2	1.883	1.895	1.824	-
Al-O3	1.700	1.690	1.701	-
Al-O4	1.711	1.708	1.694	-
H-O1	2.581	-	2.567	-
H-O2	0.985	0.982	0.964	-
H-O3'	2.037	-	2.838	-
H-O4'	2.863	-	3.274	-
H-O*	2.619	-	2.597	-
H-O*	2.790	-	3.141	-

MW denotes data from Mombourquette and Weil (1985). O^* denotes the two additional oxygen atoms around the large c-axis channel (not labeled in Figure 3.1). Also included for comparison are those for the $[AlO_4/H^+]^+$ centers.

3.3.3 $[AlO_4/Li^+]^0$ defects

The calculated minimum energy of the $[AlO_4/Li^+(a_<)]^0$ defect is 1.157 eV lower than its $[AlO_4/Li^+(a_>)]^0$ counterpart. Unlike the $[AlO_4/H^+]^0$ defects, however, distortion of the $[AlO_4/Li^+]^0$ defects is reflected by displacements of all atoms involved (Table 3.2 and Fig. 3.3). Both Li and Al atoms remain close to the 2-fold symmetry axis, but are significantly displaced along the axis.

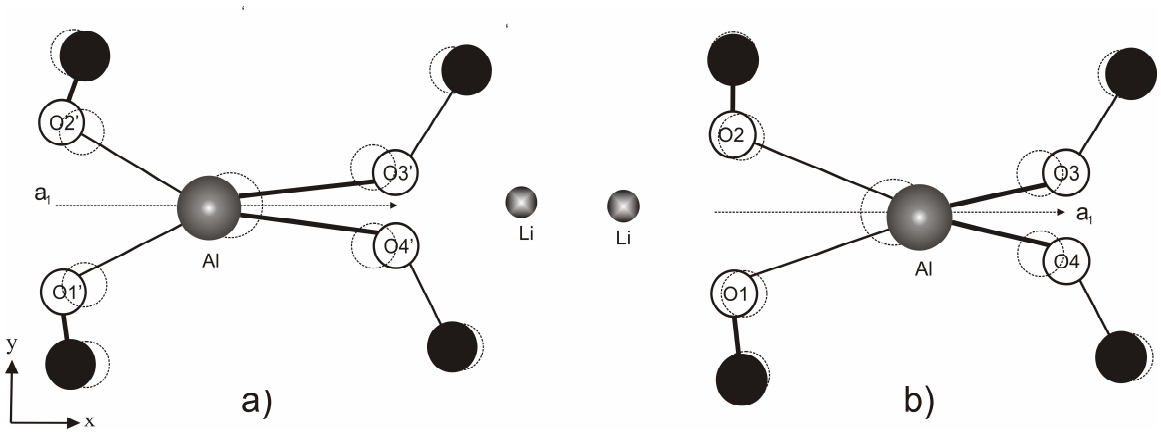

Figure 3.3: Structural models for a) $[AlO_4/Li^+(a_>)]^0$ and b) $[AlO_4/Li^+(a_<)]^0$, in comparison with the original Si and O positions of the ideal quartz structure (open circles). The original Li position (not shown) was placed at the centre of the large c-axis channel.

The Al–O bond distances in the $[AlO_4/Li^+]^0$ defects also show a different behavior from those in the $[AlO_4/H^+]^0$ defects (Table 3.4). A preservation of the C_2 symmetry for the Al site is evident in the calculated Al–O bond distances. Our calculated Al–O bond distances show that the long Si–O1 and Si–O2 bonds become the short Al–O1 and Al–O2 bonds in the $[AlO_4/Li(a_<)]^0$ defect, similar to a switch reported by Mombourquette and Weil (1985).

The Li^+ ion in $[AlO_4/Li(a_<)]^0$ has a pseudo-tetrahedral coordination: Li–O4 = Li-O3=1.87 and Li–O1' = Li–O2' =1.98 Å. The Li^+ ion in $[AlO_4/Li(a_>)]^0$ has a similar coordination environment: Li–O4 = Li–O3 = 1.9 and Li–O1'= Li–O2' = 1.98 Å. Displacements of the nearest Si neighbors to the $[AlO_4/H^+]^0$ defects are ~0.07 Å, smaller than that observed in the $[AlO_4/H^+]^0$ defects.

Table 3.4: Calculated bond distances of the $[AlO_4/Li^+]^0$ defects

	Bond distances (Å)			
	$[AlO_4/Li(a_>)^+]^0$		$[AlO_4/Li(a_>)^+]^+$	
	This study	MW	BP	MW
Al-O1'	1.711	1.687	1.730	1.663
Al-O2'	1.712	1.687	2.016	1.916
Al-O3'	1.779	1.783	1.791	1.717
Al-O4'	1.779	1.783	1.794	1.705
Li-O1	1.982	-	2.075	-
Li-O2	1.982	-	2.113	-
Li-O3'	1.902	1.672	2.053	-
Li-O4'	1.899	1.672	2.050	-
Li-O*	3.514	-	3.499	-
Li-O*	3.047	-	3.604	-
	$[AlO_4/Li(a_<)^+]^0$		$[AlO_4/Li(a_<)^+]^+$	
Al-O1	1.772	1.791	1.794	-
Al-O2	1.772	1.791	1.793	-
Al-O3	1.711	1.687	2.017	-
Al-O4	1.711	1.687	1.731	-
Li-O1	1.870	1.700	2.050	-
Li-O2	1.870	1.700	2.050	-
Li-O3'	1.985	-	2.071	-
Li-O4'	1.985	-	2.112	-
Li-O*	3.541	-	3.613	-
Li-O*	3.005	-	3.573	-

MW represents literature data from Mombourquette and Weil (1985). O^* denotes the two additional oxygen atoms around the large c-axis channel (not labeled in Figure 3.1). Also included for comparison are those for the $[AlO_4/Li^+]^+$ centers.

3.3.4 $[AlO_4/Na^+]^0$ defects

The calculated minimum energy for the $[AlO_4/Na(a_<)]^0$ defect is 3.76 eV lower than the $[AlO_4/Na(a_>)]^0$ structure. A strong repulsion between the Al^{3+}ion and the Na^+ ion is evident in both cases (Table 3.2 and Fig. 3.4). However, the largest displacement again is oriented mainly along the a-axis, maintaining the Al position close to the 2-fold

symmetry axis. Similar to the $[AlO_4/Li^+]^0$ defects, a reversal of the "long" and "short" Al-O bonds are observed for the $[AlO_4/Na^+(a_<)]^0$ structure.

Table 3.5: Calculated bond distances for the $[AlO_4/Na^+]^0$ defects

	Bond distances (Å)		
	$[AlO_4/Na(a_>)^+]^0$		$[AlO_4/Na(a_>)^+]^+$
	This study	MW	BP
Al-O1'	1.712	1.693	1.985
Al-O2'	1.721	1.691	1.730
Al-O3'	1.772	1.768	1.800
Al-O4'	1.766	1.767	1.796
Na-O1	2.247	-	2.247
Na-O2	2.226	-	2.226
Na-O3'	2.284	1.974	2.237
Na-O4'	2.161	1.952	2.222
Na- O^*	2.638	-	3.522
Na- O^*	2.567	-	3.540
	$[AlO_4/Na(a_<)^+]^0$		$[AlO_4/Na(a_<)^+]^+$
Al-O1	1.775	-	1.803
Al-O2	1.764	-	1.800
Al-O3	1.721	-	1.966
Al-O4	1.713	-	1.730
Na-O1	2.171	-	2.220
Na-O2	2.132	-	2.231
Na-O3'	2.221	-	2.229
Na-O4'	2.249	-	2.247
Na-O^*	3.375	-	3.577
Na-O^*	2.980	-	3.527

For both structures, displacements of the nearest Si atoms to the AlO_4 tetrahedron are up to 0.15 Å, again similar in magnitude to the displacements of the substitutional Al atom but larger than those observed in $[AlO_4/H^+]^0$ and $[AlO_4/Li^+]^0$ defects .

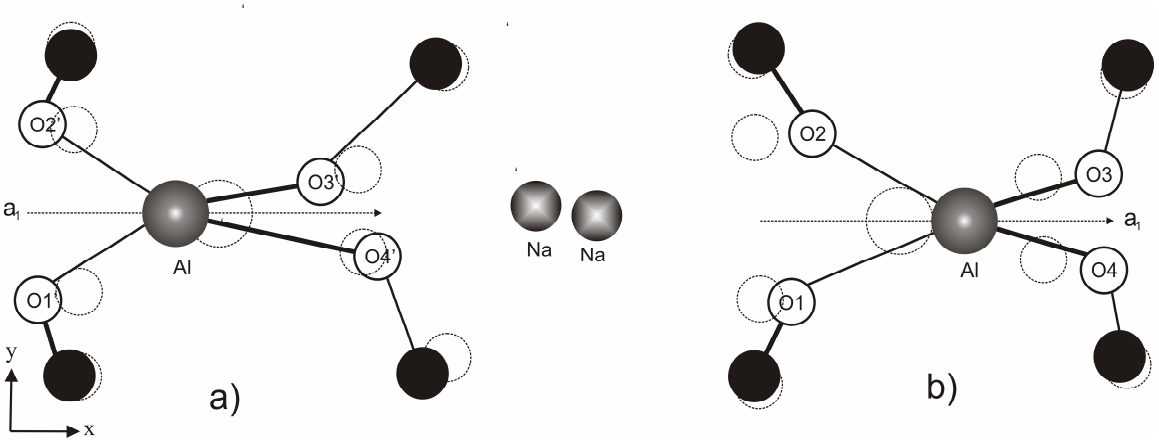

Figure 3.4: Structural models for a) $[AlO_4/Na^+(a_>)]^0$ and b) $[AlO_4/Na^+(a_<)]^0$, in comparison with the original Si and O positions of the ideal quartz structure (open circles). The original Na position (not shown) was placed at the centre of the large c-axis channel.

3.3.5 $[AlO_4/K^+]^0$ defects

The calculated minimum energy for the $[AlO_4/K(a_>)]^0$ defect is 1.154 eV lower than the $[AlO_4/K(a_<)]^0$ structure. The strong repulsion between Al^{3+} and K^+ can be observed (Table 3.2 and Fig. 3.5), similar to those observed in the $[AlO_4/Li]^0$ and $[AlO_4/Na]^0$ defects. The $[AlO_4/K(a_<)]^0$ structure maintains its Al atom on the 2-fold symmetry axis but with a significant displacement along the axis. The $[AlO_4/K(a_>)]^0$ defect, however, shows a large displacement of Al away from the 2-fold symmetry axis, as well as a displacement of K^+ from the centre of the c-axis channel (Table 3.2 and Fig. 3.5). The nearest Si atoms are significantly displaced, up to 0.15 Å.

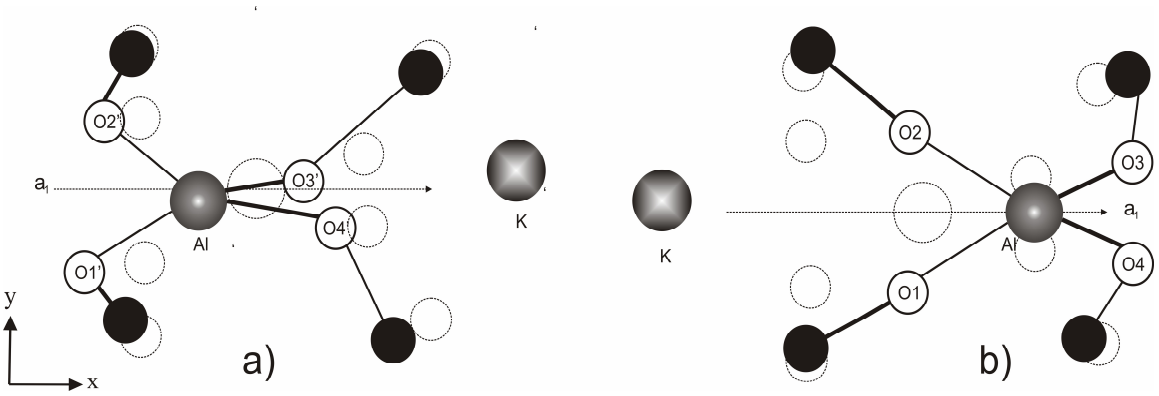

Figure 3.5: Structural models for a) $[AlO_4/K^+(a_>)]^0$ and b) $[AlO_4/K^+(a_<)]^0$, in comparison with the original Si and O positions of the ideal quartz structure (open circles). The original K position (not shown) was placed at the centre of the large c-axis channel.

Table 3.6: Calculated bond distances for the $[AlO_4/K^+]^0$ defects

Bond distances (Å)			
$[AlO_4/K(a_>)^+]^0$		$[AlO_4/K(a_<)^+]^0$	
Al-O1'	1.711	Al-O1	1.761
Al-O2'	1.724	Al-O2	1.760
Al-O3'	1.778	Al-O3	1.727
Al-O4'	1.764	Al-O4	1.727
K-O1	2.500	K-O1	2.498
K-O2	2.640	K-O2	2.496
K-O3'	2.585	K-O3'	2.585
K-O4'	2.467	K-O4'	2.585
K-O*	2.649	K-O*	2.996
K-O*	2.705	K-O*	2.854

O* denotes the two additional oxygen atoms around the large c-axis channel (not labeled in Figure 1).

3.4 Discussion

3.4.1 Comparison with previous theoretical studies

The present DFT calculations with 72-atom supercells have resulted in a number of notable improvements relative to previous theoretical studies (Mombourquette and Weil, 1985; Leslie, 1989; Cora and Pisani, 1994). For example, Mombourquette and Weil (1985) reported only small differences in minimum energy between the $[AlO_4/M^+(a_<)]^0$ and $[AlO_4/M^+(a_>)]^0$,(M=H, Li) defects and that the latter is slightly more stable than the former. These results, if correct, would result in the formation of two types of paramagnetic centres ($[AlO_4/M^+(a_<)]^+$ and $[AlO_4/M^+(a_>)]^+$), with the former being somewhat more common. However, EPR experiments show that the $[AlO_4/M^+(a_>)]^+$ centres are commonly observed (Mackey 1963; Mackey et al., 1972; Nuttall and Weil, 1981a,b, Dickson and Weil, 1990; Howarth et al., 1997). The results of Cora and Pisani (1994) as well as those of Leslie (1989) suggest $[AlO_4/Li^+(a_>)]^0$ and $[AlO_4/Na^+(a_<)]^0$ to be the energetically preferred configurations, implying again that the paramagnetic species predominantly observed should be $[AlO_4/Li^+(a_<)]^+$ and $[AlO_4/Na^+(a_>)]^+$. Our results show that the $[AlO_4/M^+(a_<)]^0$ defects are more stable for M=H, Li and Na (i.e. ΔE=0.943 eV, 1.157 eV and 3.76 eV for H, Li and Na, respectively), consistent with observations from EPR experiments. Also, our results predict the $[AlO_4/K^+(a_<)]^+$ configuration to be energetically preferred, but no EPR data are available to test this prediction.

Our calculated bond distances for the $[AlO_4/H^+]^0$ defects are similar to those of Mombourquette and Weil (1985). However, differences are obvious for the $[AlO_4/Li^+]^0$ and $[AlO_4/Na^+]^0$ defects (Tables 3.4 and 3.5). For example, our calculated Li-O and Na-O bond distances are significantly longer than those obtained by Mombourquette and Weil

(1985) and are in better agreements with experimental Li-O and Na-O bond distances from X-ray diffraction experiments (e.g. Wenger and Armbruster, 1991, Wood and Palenik, 1999).

3.4.2 Comparison between the $[AlO_4/M^+]^0$ defects and their paramagnetic derivatives

Table 3.2 shows that significant differences exist between the $[AlO_4/M^+]^+$ paramagnetic centres and their respective diamagnetic precursors and that the magnitude of difference is dependent on the charge compensator. For example, the AlO_4 tetrahedra associated with those having H as the compensator show very small differences. However, dramatic differences are present between the Li- and Na-compensated defects and their paramagnetic derivatives. For example, the largest deviations of $[AlO_4/Li^+(a_<)]^+$ and $[AlO_4/Na^+(a_<)]^+$ centres from their diamagnetic precursors involve the O3 and O4 atoms, which move close to the a-axis, almost aligning their positions on the c-axis direction. As a result, they form pseudo-tetrahedral "cages" along with the O1' and O2' located on the other side of the c-axis channel, in which the Li^+ and Na^+ ions are accommodated. Similar distortions of the AlO_4 tetrahedra are observed for the $[AlO_4/Li^+(a_>)]^+$ and $[AlO_4/Na^+(a_>)]^+$ centres as well (Table 3.2).

Differences between the diamagnetic defects and their paramagnetic derivatives are also evident in the Al-O and M-O bond distances (Tables 3.3 to 3.5). As noticed before, relaxation involving the $[AlO_4/H^+]^+$ centres is minimal; the Al-O and H-O bond distances remain very close to those in the diamagnetic precursors. However, large variations in Al-O, Li-O and Na-O bond distances are obvious in the $[AlO_4/Li^+]^{0/+}$ and

$[AlO_4/Na^+]^{0/+}$ defects (Table 3.4 and Table 3.5). Particularly, the oxygen atom with hole trapping is characterized by an increased Al-O bond distance but decreased Li-O and Na-O values.

3.4.3 Implications for uptake of Al in quartz

The developments of microbeam techniques (e.g. EMPA, FTIR, LA-ICPMS, PIXE and SIMS) for in-situ analyses, combined with textural relationships as revealed by cathodoluminescence (CL) and back-scattered electron (BSE) imaging, have resulted in an increasingly large database of high-quality Al, H, Li, Na, K and other trace elements in quartz from a wide range of geological environments (e.g. Smith and Steele, 1984; Perny et al., 1992; Demars et al., 1996; Watt et al., 1997; Götze and Plötze, 1997; Flem et al., 2002; Hongu et al., 2002; Müller et al., 2003; Götze et al., 2004, 2005; Landtwing and Pettke, 2005; Miyoshi et al., 2005; Rusk et al., 2006; Müller et al., 2008). This database has removed uncertainties in previous bulk analyses (e.g. Dennen et al., 1970; Scotford, 1975) and has clearly demonstrated that the uptake of Al in quartz is a complex function of both fluid/melt chemistry and physical conditions (e.g. temperature and growth rates), different from the temperature dependence of Ti uptake in this mineral (Wark and Watson, 2006). This dependence of Al uptake on fluid/melt chemistry is readily attributable to complex charge-coupled substitutions involved. The most dominant type of charge-coupled substitutions for Al uptake in quartz is $Al^{3+} + M^+ = Si^{4+}$, where M = H, Li, Na and K in the c-axis channels, while other substitutions involving P^{5+} or silicon vacancy have also been suggested but are generally less important (e.g. Smith and Steele, 1984; Perny et al., 1992; Watt et al., 1997; Götze et al., 2004; Müller et al.,

2008). Therefore, this present study on the $[AlO_4/M^+]^0$ defects has direct relevance for better understanding of the uptake of Al in quartz.

First of all, the present study shows that the $[AlO_4/M^+]^0$ defects differ from their respective paramagnetic centres in both the locations of the monovalent cations and the geometries of the $[AlO_4]$ groups. Therefore, the $[AlO_4/M^+]^+$ paramagnetic centres as characterised by EPR studies, while confirming the charge-coupled substitutions, do not provide a direct picture about the local structural environments of their diamagnetic precursors.

Secondly, chemical analyses have shown that H^+, Li^+ and Na^+ ions play dominant roles in the uptake of Al in quartz, particularly those of hydrothermal origins (Perny et al., 1992; Miyoshi et al., 2005; Branlund and Hofmeister, 2007). Elevated K contents (and positive correlations with Al) have also been documented in a variety of natural quartz (e.g. those from volcanic rocks, pegmatites and porphyry copper deposits; Watt et al., 1997; Rusk et al., 2006; Müller et al., 2008). Unlike the $[AlO_4/H^+]^+$, $[AlO_4/Li^+]^+$ and $[AlO_4/Na^+]^+$ paramagnetic centres, however, $[AlO_4/K^+]^+$ paramagnetic centres have not been observed by EPR spectroscopy. Our DFT calculations show that the $[AlO_4/K^+]^0$ defects (and $[AlO_4/K^+]^+$ paramagnetic centres as well) are stable in quartz, hence supporting the role of K in the uptake of Al. However, detection of the $[AlO_4/K^+]^+$ paramagnetic centres by conventional EPR techniques is expected to be difficult, because its characteristic ^{39}K superhyperfine structure is expected to be very small (i.e. ~0.002 mT) owing to the minuscule $g_n(^{39}K)$ value of 0.26099. Therefore, other experimental techniques such as electron nuclear double resonance (ENDOR) and electron spin echo envelope modulation (ESEEM) spectroscopy, which are more sensitive to small

hyperfine structures, may be required to detect and characterise the $[AlO_4/K^+]^+$ centres in quartz.

Thirdly, monovalent ions other than H^+, Li^+, Na^+ and K^+ may contribute to the uptake of Al in quartz from specific cases as well. For example, EPR studies have identified $[AlO_4/Ag^+]^+$, $[AlO_4/Ag_2^+]^+$, and $[AlO_4/Cu^+]^+$ centres in quartz (Weil, 1984). Also, Ag^+ and Cu^+ ions are stable in the form of various complexes and are known to reach elevated concentrations in some mineralization fluids (Robb, 2004; Sherman, 2007). Therefore, Ag^+ and Cu^+ ions are expected to participate in the uptake of Al in quartz from some mineral deposits.

Fourthly, several studies have also documented anomalous relationships between Al^{3+} and $\Sigma(H^+ + Li^+ + Na^+ + K^+)$ (i.e., lack of positive correlation or excess monovalent cations relative to Al^{3+}) in quartz (e.g. Hervig and Peacock, 1989; Branlund and Hofmeister, 2007). EPR studies have established numerous paramagnetic centres with monovalent ions (e.g., H^+ and Li^+) not associated with Al^{3+} (e.g. atomic hydrogen and lithium H^0 and Li^0, hydrogarnet-type centres $[H_4O_4]^+$ and $[H_3O_4]^0$, and other impurity-related centres such as $[FeO_4/H^+]^0$, $[FeO_4/Li^+]^0$, $[TiO_4/H^+]^0$, $[TiO_4/Li^+]^0$, $[TiO_4/Na^+]^0$, $[GeO_4/Li^+]^0$ and $[GeO_4^+/H^+]^0$; Weil, 1984; 2000; Lees et al., 2003). Of these, atomic hydrogen and lithium in quartz have been suggested to form from the $[AlO_4/H^+]^0$ and $[AlO_4/Li^+]^0$ defects during irradiation. Similarly, Götze et al. (2005) suggested that redistribution of alkali ions from diamagmetic $[AlO_4/Li^+]^0$ defects may have been responsible for the formation of $[TiO_4/Li^+]^0$ and $[GeO_4/Li^+]^0$ centres during irradiation. Nevertheless, the H^+ and alkali ions in hydrogarnet-type defects and those in Fe-related

defects are not associated with Al and, therefore, may account for observed anomalous relationships (Hervig and Peacock, 1989; Branlund and Hofmeister, 2007).

Finally, the presence of Al and other impurities in quartz is known to exert important influences on various types of physical and chemical properties of this mineral. For example, Branlund and Hofmeister (2007) documented significant effects of impurities on thermal diffusion and heat transfer in quartz and called for better data on the locations of impurities in quartz. The present study on the stabilities, locations and geometries of the $[AlO_4/M^+]^0$ defects provides new insights into the effects of impurities on diffusion processes. For example, the differences in both the locations and bonding environments among H^+, Li^+, Na^+, K^+ are responsible for their contrasting diffusion rates (see also Mombourquette and Weil, 1985). Likewise, the significant distortions in the c-axis channels are also expected to contribute to the observed differences in diffusion rates.

3.5 References

Allan, D.C. and Teter, M.P. (1990) Local density approximation total energy calculations for silica and titania structure and defects. Journal of American Ceramic Society, 73: 3247-3250

Branlund, J.M. and Hofmeister, A.M. (2007) Thermal diffusivity of quartz to 1,000ºC: Effects of impurities and the α-β phase transition. Physics and Chemistry of Minerals, 34: 581-595

Chelikowsky, J.R., King, H.E., Troullier, N., Martins, J.L. and Glinnemann, J. (1990) Structural properties of α-quartz near the amorphous transition. Physical Review Letters, 65: 3309-3312

Civalleri, B., Ferrari, A.M., Llunell, M., Orlando, R., Merawa, M. and Ugliengo, P. (2003) Cation selectivity in alkali-exchanged chabazite: an ab-initio periodic study. Chemistry of Materials: 15, 3996-4004

Cohen, A.J. (1956) Color centers in the alpha-quartz called amethyst, The American Mineralogist, 41: 874-891

Cora, F. and Pisani, C. (1994) A quantum-mechanical ab-initio simulation of neutral and charged point-defects in alpha-quartz. Modelling and Simulation in Material Science and Engineering, 2: 965-974

Dennen, W.H., Blackbut, W.H. and Quesada, A. (1970) Aluminum in quartz as a geothermomether. Contributions to Mineralogy and Petrology: 27, 332-342

Demars, C., Pagel, M., Deloule, E. and Blanc, P. (1996) Cathodoluminescence of quartz from sandstones: Interpretation of the UV range by determination of trace element distributions and fluid-inclusion P-T-X properties in authigenic quartz. American Mineralogist, 81: 891-901

Dickson, R.S. and Weil, J.A. (1990) The magnetic properties of the oxygen-hole aluminum centres in crystalline SiO_2. IV. [AlO_4/Na^+]. Canadian Journal of Physics, 68: 630-642

Dovesi, R., Ermondi, E., Ferrero, E., Pisani, C. and Roetti, C. (1983) Hartree-Fock study of lithium hydride with the use of a polarizable basis set, Physical Review B, 29: 3591-3600.

Dovesi, R., Pisani, C., Roetti, C. and Silvi, B. (1987) The electronic structure of α-quartz: A periodic Hartree-Fock calculation. Journal of Chemical Physics, 86: 6967-6971.

Dovesi, R., Roetti, C., Freyria Fava, C., Prencipe, M. and Saunders, V.R.(1991) On the elastic properties of lithium, sodium an potassium oxide. An ab initio study, Chemical Physics 156: 11-19

Dovesi, R., Saunders, V.R., Roetti, C., Orlando, R., Zicovich-Wilson C.M., Pascale F. Civalleri B., Doll K., Harrison N.M., Bush I.J., D'Arco P. and Llunnell M. (2006) CRYSTAL2006, User's Manual; http://www.crystal.unito.it, University of Torino, Torino

Flem, B., Larsen, R.B., Grimstvedt, A. and Mansfeld, J. (2002) In situ analysis of trace elements in quartz by using laser ablation inductively coupled plasma mass spectrometry. Chemical Geology, 182: 237-247

Gnani, E., Reggiani, S., Colle, R. and Rudan, M. (2000) Band-structure calculations of SiO_2 by means of Hartree-Fock and density-functional techniques. IEEE Transactions on electron devices, 47: 1795-1803

Götze, J. and Plötze, M. (1997) Investigation of trace-element distribution in detrital quartz by electron paramagnetic resonance (EPR). European Journal of Mineralogy, 9: 529–537

Götze, J., Plötze, M., Graupner, T., Hallbauer D.K. and Bray, C.J. (2004) Trace element incorporation into quartz: a combined study by ICP-MS, electron spin resonance, cathodoluminescence, capillary ion analysis, and gas chromatography. Geochimica et Cosmochimica Acta, 68: 3741–3759

Götze, J., Plötze, M., Tichomirowa M., Fuchs H. and Pilot J. (2001) Aluminium in quartz as an indicator of the temperature of formation of agate. Mineralogical Magazine, 65: 407-413

Götze, J., Plötze, M. and Trautmann, T. (2005) Structure and luminescence characteristics of quartz from pegmatites. American Mineralogist, 90: 13-21

Griffiths, J.H.E., Owen, J. and Ward, E.M. (1954) Paramagnetic resonance in neutron irradiated diamond and smoky quartz. Nature, 174: 439-440

Hervig, R.L. and Peacock, S.M. (1989) Implications of trace element zoning in deformed quartz from the Santa Catalina mylonite zone. The Journal of Geology, 89: 343-350

Hongu, H., Yoshiasa, A., Kurosawa, M., Ohkawa, M., Kitagawa, R. and Takeno, S. (2002). High Al contents in quartz and hydrothermal alteration of the "Roseki" deposits in the Mitsuishi district, Southwest Japan. Journal of Mineralogical and Petrological Sciences, 97: 168-176

Howarth, D.F., Mombourquette, M.J. and Weil, J.A. (1997) The magnetic properties of the oxygen-hole aluminum centers in crystalline SiO_2. V. ^{17}O-enriched $[AlO_4/Li]^+$ and dynamics thereof. Canadian Journal of Physics, 75: 99-115

Kronenberg, A.K. (1994) Hydrogen speciation and chemical weakening of quartz. In: Heaney PJ, Prewitt CT, Gibbs VV (eds) Silica: Physical behavior, geochemistry and materials applications. Reviews in Mineralogy, 29: 123–176

Landtwing, M.R. and Pettke, T. (2005) Relationships between SEM-cathodoluminescence response and trace-element composition of hydrothermal vein quartz. American Mineralogist, 90: 122-131

Lee, C, Yang, W. and Parr, RG (1988) Development of the Colle-Salvetti correlation-energy formula into a functional of the electron density. Physical Review B, 37: 785-789.

Lees, N.S., Walsby, C,J., Williams, J.A.S., Weil, J.A. and Claridge, R.F.C. (2003)
EPR of a hydrogen/ double-lithium centre in α-quartz. Physics and Chemistry of Minerals, 30: 131–141

Le Page, Y., Calvert, L.D. and Gabe, E.J. (1980) Parameter variation in low quartz between 94 and 298 K. Journal of Physics and Chemistry of Solids, 41: 721-725

Leslie, M. (1989) Calculation pf the energies of point defects in quartz. Journal of the Chemical Society-Faraday Transactions II, 89: 407-413

Liu, F., Garofalini, S.H., King-Smith, D. and Vanderbilt, D. (1994) First-principles study of crystalline silica, Physical Review B, 49: 12528-12534

Mackey, J.H. (1963) ERP study of impurity-related color centers in germanium-doped quartz. The Journal of Chemical Physics, 39: 74-83

Mackey, J.H., Boss, J.W. and Wood, D.E. (1970) EPR study of substitutional-aluminum-related hole centers in synthetic α-quartz. Journal of Magnetic Resonance, 3: 44-54

Merawa, M., Labeguerie, P., Ugliengo, P., Doll K. and Dovesi R. (2004) The structural, electronic and vibrational properties of LiOH and NaOH: an ab initio study,
Chemical Physics Letters, 387: 453-459

Miyoshi, N., Yamaguchi, Y. and Makino, K. (2005) Successive zoning of Al and H in hydrothermal vein quartz. American Mineralogist, 90: 310-315

Mombourquette, M.J. and Weil, J.A. (1985) Ab initio self-consistent-field molecular-orbital calculations on AlO_4 centers in alpha-quartz. II. Canadian Journal of Physics, 63: 1282-1293

Monkhorst, H.J. and Pack, J.D. (1976) Special points for Brillouin-zone integrations. Physical Review B, 13: 5188-5192

Montanari, B., Civalleri, B., Zicovich-Wilson, C.M. and Dovesi R. (2006) Influence of the exchange-correlation functional in all-electron calculations of the vibrational

frequencies of corundum (alpha-Al2O3), International Journal of Quantum Chemistry 106: 1703-1714

Müller, A., Wiedenbeck, M., Van Den Kerkhof, A.M., Kronz, A. and Simon, K. (2003) Trace elements in quartz – a combined electron microprobe, secondary ion mass spectrometry, laser-ablation ICP-MS, and cathodoluminescence study. European Journal of Mineralogy, 15: 747-763

Müller, A., Ihlen, P.M. and Kronz, A. (2008) Quartz chemistry in polygeneration Sveconorwegian pegmatites Froland, Norway. European Journal of Mineralogy, 20: 447-463

Nada, R., Catlow, C.R.A., Dovesi, R. and Pisani, C. (1990) An Ab-Initio Hartree-Fock Study of alpha-Quartz and Stishovite, Physics and Chemistry of Minerals, 17: 353-362

Nilges, M.J., Pan, Y.M. and Mashkovtsev, R.I (2008) Radiation-damage-induced defects in quartz. I. Single-crystal W-band EPR study of hole centers in an electron-irradiated quartz. Physics and Chemistry of Minerals, 35: 103-115

Nilges, M.J., Pan, Y.M. and Mashkovtsev, R.I (2009) Radiation-damage-induced defects in quartz. III. Single-crystal W-band EPR, ENDOR and ESEEM study of a peroxy radical. Physics and Chemistry of Minerals, 36, (in press)

Nuttall, R.H.J. and Weil, J.A. (1981a) The magnetic properties of the oxygen-hole aluminum centers in crystalline SiO_2. I. $[AlO_4]^+$, Canadian Journal of Physics, 59: 1886-1892

Nuttall, R.H.J. and Weil, J.A. (1981b) The magnetic properties of the oxygen-hole aluminum centers in crystalline SiO_2. II. $[AlO_4/H^+]^+$ and $[AlO_4/Li^+]^+$, Canadian Journal of Physics, 59: 1709-1718

Pacchioni, G., Frigoli, F., Ricci, D. and Weil, J.A. (2001) Theoretical description of hole localization in a quartz Al center: The importance of exact electron exchange, Physical Review B, 63: 054102

Pan, Y.M., Nilges, M.J. and Mashkovtsev, R.I (2008) Radiation-induced defects in quartz. II. Single-crystal W-band EPR study of a natural citrine quartz. Physics and Chemistry of Minerals, 35: 387-397

Pankrath, R. (1991) Polarized IR spectra of synthetic smoky quartz. Physics and Chemistry of Minerals, 17: 681-9

Perny, B., Eberhardt, P., Ramseyer, K., Mullis, J. and Pankrath, R. (1992) Microdistribution of Al, Li and Na in α quartz: possible causes and correlation with short-lived cathodoluminescence. American Mineralogist, 77: 534-544

Robb, L.J. (2004) Introduction to Ore-Forming Processes. John Wiley & Sons, 384p.

Rusk, B.G., Reed, M.H., Dilles, J.H. and Kent, A.J.R. (2006) Intensity of quartz cathodoluminescence and trace-element content in quartz from the porphyry copper deposit at Butte, Montana. American Mineralogist, 91: 1300-1312

Schnadt, R. and Schneider, J. (1971) The electronic structure of the trapped-hole center in smoky quartz. Physics of Condensed Matter, 11: 19-42

Scotford, D.M. (1975) Test of aluminum in quartz as a geothermometer, American Mineralogist, 60: 139-142

Sherman, D.M. (2007) Complexation of Cu^{+} in hydrothermal NaCl brines: ab initio molecular dynamics and energetics. Geochimica et Cosmochimica Acta, 71: 714-722

Smith, J.V. and Steele, I.M. (1984) Chemical substitution in silica polymorphs. Neues Jahrbuch fur Mineralogie Abhandlungen, 3: 137-144

To, J., Sokol, A.A., French, S.A., Kaltsoyannis, N. and Catlow, R. (2005) Hole localization in $[AlO_4]^0$ defects in silica materials. The Journal of Chemical Physics, 122: 144704

Walsby, C.J., Less, N.S., Claridge, R.F.C and Weil, J.A. (2003) The magnetic properties of oxygen-hole aluminum centers in crystalline SiO_2. VI. A stable AlO_4/Li centre, Canadian Journal of Physics, 81: 583-598

Wark, D.A. and Watson, E.B. (2006) TitaniQ: a titanium-in-quartz geothermometer. Contributions to Mineralogy and Petrology, 152: 743-754

Watt, G.R., Wright, P., Galloway, S. and McLean, C. (1997) Cathodoluminescence and trace element zoning in quartz phenocrysts and xenocrysts. Geochimica et Cosmochimica Acta, 61: 4337-4348

Weil, J.A. (1984) A review of electron spin spectroscopy and its applications to the study of paramagnetic defects in crystalline quartz. Physics and Chemistry of Minerals, 10: 149-165

Weil, J.A. (2000) A demi-century of magnetic defects in α-quartz. In Defects in SiO_2 and Related Dielectrics: Sciences and Technology (Pacchioni G, Skuja L, Griscom DL eds), Kluwer Academic, Netherlands, 197-212

Wenger, M. and Armbruster, T. (1991) Crystal chemistry of lithium: oxygen coordination and bonding. European Journal of Mineralogy, 3: 387-399

Wood, R.M. and Palenik, G.J. (1999) Bond valence sums in coordination chemistry. Sodium-oxygen complexes. Inorganic Chemistry, 38: 3926-3930

Chapter 4

Modeling of [AlO_4/Li] paramagnetic defects in α-quartz

The [AlO_4/Li] paramagnetic defects in α-quartz have been investigated by *ab initio* calculations at the density functional theory (DFT) level, using 72 and 108 atom supercells, and all-electron basis sets. Our results show that the Al-Li coupled substitution could give rise to three distinct paramagnetic defects, two of them having the hole located on a short-bonded O and one trapping the hole on a long-bonded O atom. The structural models from our calculations are $[AlO_4/Li^+(a_<)]^+$, $[AlO_4/Li^+(a_>)]^+$ and $[AlO_4/Li^+(c_{small})]^+$ with $a_<$, $a_>$ and c_{small} indicating the position of the Li^+ ion. The present study clarifies the ambiguities related to the structural model of the $[AlO_4/Li]^q$ center, discovered and proposed by Walsby et al. (2003), and eliminates the uncertainties related to the charge of the compensating Li ion. Our results provide a structural model for the Li-compensated defect observed by Walsby et al. (2003) in good agreement with the experimentally determined EPR parameters. We also suggest an additional paramagnetic defect $[AlO_4/Li^+(c_{small})]^+$, with the unpaired electron located on a short-bonded O atom and the Li compensator just off the edge of the small channel. However the structural similarities with the $[AlO_4/Li^+(a_>)]^+$ defect would require detection and measurement of the ^{17}O hyperfine structure for an unequivocal EPR identification.

4.1 Introduction

The important technological applications of quartz as well as the ability of the defect centers to alter its electronic, mechanical and other properties have always attracted the interest of the scientific community. The structural study of defect centers in quartz began as early as 1950s (Weil, 1984; 2000), and quartz provides an ideal host for electron paramagnetic resonance (EPR) studies of point defects.

In spite of its natural tendency to occur as a very pure material, crystalline quartz usually contains small concentrations (ppm) of impurity elements, aluminum being by far the most common of them (Frondel, 1962; Weil, 1984).

The incorporation of aluminum in quartz is taking place at the Si site due to the similar size of the two ions and it is generally accompanied by charge compensation with monovalent ions such as H^+, Li^+ and Na^+ (Mackey, 1963; 1970; Nuttall and Weil, 1981; Dickson and Weil, 1990). This coupled substitution gives rise to a class of diamagnetic defects, (i.e $[AlO_4/M^+]^0$), which upon irradiation at low temperature ($T \leq 100$ K) (Mackey, 1963) with x-rays or γ-rays become paramagnetic (i.e. $[AlO_4/M^+]^+$) and can be easily studied by standard EPR spectroscopy.

$[AlO_4/M^+]^+$ paramagnetic defect centers in quartz were first observed by Mackey (1963) in quartz samples irradiated and measured at 77 K. Subsequent EPR studies (Mackey et al., 1970; Nuttall and Weil, 1981; Howarth et al., 1998) reported the presence of $[AlO_4/H^+]^+$, $[AlO_4/Li^+]^+$, and $[AlO_4/Na^+]^+$ centers. Based on the spin Hamiltonian parameters the compensating cations were located in the hexagonal channels running parallel to c-axis, in opposition with a short-bonded oxygen that traps the hole.

Although the structural model of $[AlO_4/M^+]^+$ defect centers seemed to be clearly defined, the findings of Walsby et al. (2003) opened a novel controversy. A new type of $[AlO_4/Li]$ center was reported, different from the one observed before. The new center was called $[AlO_4/Li]^q$ due to the uncertainties regarding the charge of Li and therefore the overall charge of the defect. Based on the orientation of the **g** and **A**(^{27}Al) matrices it was concluded that unlike the case of the $[AlO_4/Li^+]^+$ defect, the unpaired electron was located on a long-bonded oxygen atom. Using the ^{7}Li superhiperfine, Walsby et al. (2003) determined the distance between the oxygen atom containing the unpaired electron and the Li^+ ion to be in the range of 3.4-3.9 Å, results which gave 2 possible locations for Li^+: a) a site close to the center of one of the two large c-axis channels and b) a site on the edge of one of the smaller channels.

A possible explanation, suggested by the authors for the existence of the second type of $[AlO_4/Li]$ center was the possibility of compensation with an alkalide anion Li^-, similar to the well known Na^- and K^- ions (Dye and DeBacker, 1987). Contrary to this model, the *ab-initio* study of Brazzelli et al. (2004) regarding the stability of H^- and Li^- in silica networks concluded that Li^- ion in silica is unstable, loses the extra electron and transforms into a Li atom which becomes coordinated to a Si-O bond.

Therefore, even though detailed experimental EPR data exists on $[AlO_4/Li^+]^+$ (Nuttall and Weil, 1981; Howarth et al., 1997) and $[AlO_4/Li]^q$ (Walsby et al., 2003) we lack a structural model for the $[AlO_4/Li]^q$ defect center and a clear understanding of the formation mechanism for the two types of Li-compensated defect centers in quartz.

Accordingly, this contribution reports on a periodic *ab-initio* calculation on the $[AlO_4/Li]$ paramagnetic defect centers in quartz with focus on their geometry, electronic

structure and magnetic properties. The present study evaluates the structural models previously proposed in the literature on the basis of experimental findings.

4.2 Computational details

Several *ab-initio* calculations on Al-related defect centers in quartz have been reported in the literature (Mombourquette et al., 1984; 1985; 1986; Sim et al., 1991; Zhang and Ong, 1995; Cora and Pisani, 1995; Continenza and Di Pomponio, 1996; Pachioni et al., 2001; Laegsgaard and Stokbro, 2001; To et al., 2005; Sicolo et al., 2007). Nonetheless, most of the theoretical studies have been devoted to the $[AlO_4]^0$ defect center due to the uncertainties and controversial results related to the hole localization. Pacchioni et al. (2001) have shown that caution is necessary when using DFT methods for the study of localized holes in insulators due to the non-exact treatment of exchange and the self-interaction problem, and suggested as a solution to this problem the use of unrestricted Hartree-Fock (UHF) approach. In spite of the problems, the use of DFT approximation is desired over UHF due to its higher accuracy in determining properties such as bond dissociation and the energetic of reactions (To et al., 2005). A solution to this challenge was found by using hybrid functionals, in which the HF exchange is partly mixed with the DFT exchange (i.e. B3LYP, B3PW, etc). $[AlO_4]^0$ center in quartz is however one special case in which particular attention has to be paid to the weight of HF exchange. Sicolo et al. (2007) have obtained very good results for the calculations on the structure of the self-trapped holes in quartz, when using 50% HF exchange in the hybrid functional.

The case of [AlO_4/Li] paramagnetic centers does not seem to present the same challenges. The hole localization is easily attained using one of the very popular B3LYP functional, in which 20% of the HF exchange is mixed with 80% of DF exchange, combined with a non-local expression for the correlation, proposed by Lee et al. (1988).

All calculations were performed with the CRYSTAL06 code (Dovesi et al., 2006), which is based on local Gaussian-type orbitals. The code has the ability to compute the electronic structures and properties of periodic systems by use of the Hartree-Fock (HF), DFT and various hybrid approximations.

All electron basis sets were used for all the atoms. The basis sets used for Si and O were previously reported by Nada et al. (1990) while the basis sets used for Al and Li where the one described by Montanary et al. (2006) and Merawa et al. (2004).

The exchange-correlation contribution is the result of a numerical integration of the electron density and its gradient performed over a grid of points. In order to obtain high accuracy energy calculation and geometry optimization a pruned grid consisting of 75 radial points and 434 angular points was used (LGRID). The high accuracy grid is recommended for high accuracy energy calculations and geometry optimization (Dovesi et al., 2006). We adopted the CRYSTAL06 default thresholds for the evaluation of mono- and bielectronic integrals as well as for the geometry optimization process (Dovesi et al., 2006).

The isolated defect situation was simulated using the supercell approach. Special attention was paid in choosing the size of the supercell, which must be large enough to reduce the defect-defect interaction. Accordingly the convergence of defect-related properties (i.e. spin density and hyperfine constants) has been carefully investigated with

respect to the supercell size. We present result from calculations employing both 72 and 108 atoms supercells which allow comparison between the calculated properties as a function of defect-defect interaction.

The Pack-Monkhorst scheme (Monkhorst and Pack, 1976) for 8*8*8 k-point mesh in the Brillouin zone was applied for calculations of the bulk structure and a 4*4*4 k-point mesh was applied for calculations on the supercell.

4.3. Results

4.3.1 Quartz – bulk electronic structure

For the purpose of the present study it is beneficial to take a look at the bulk structure of quartz. In pure α-quartz (Fig 4.1), each Si atom is located at the center of a distorted oxygen tetrahedron, creating a network of linked SiO_4 units. The arrangement of the distorted tetrahedra produces two types of channels of two different diameters, which run parallel to c-axis. The channels are known as the large and the small channels (Fig 4.1).

It is also important to note that the distortion of the SiO_4 tetrahedra is given by the inequality between the Si-O bond lengths. Two of the Si-O bonds are "short" and two are "long" (1.610 and 1.614 Å at 94 K, cf LePage et al., 1980). For simplicity and easy comparison with the experimental data we will use the symbols introduced by Howarth et al. (1997) to label the two types of Si-O bonds: $Si\text{-}O_<$ and $Si\text{-}O_>$.

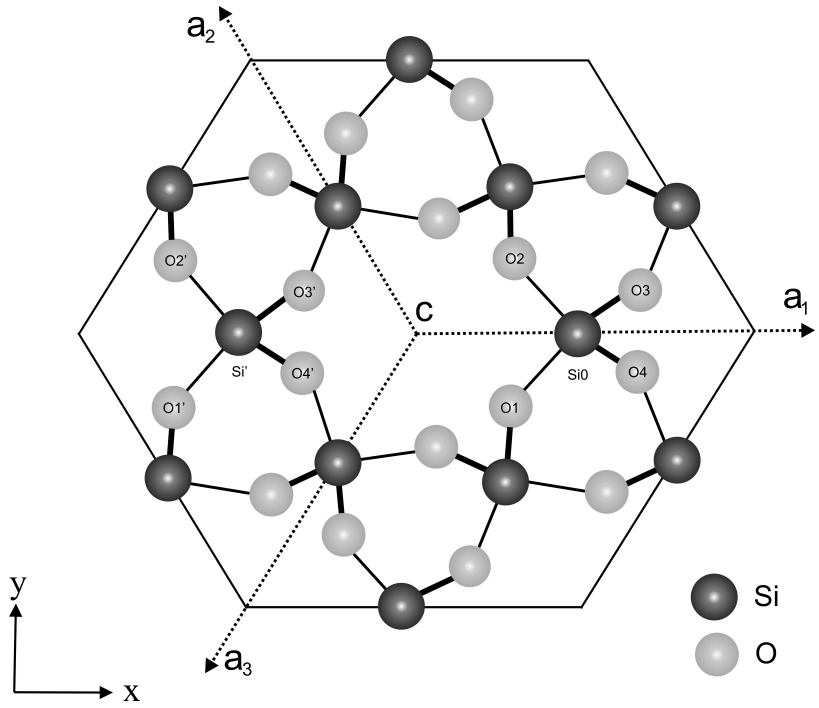

Figure 4.1: Structure of α-quartz ($P3_221$) projected on (0001) showing the large central c-axis channel surrounded by six smaller channels also parallel to the c-axis. The three axes a_1, a_2, and a_3 are indicated and the long bonds, Si-$O_>$ are marked by thick lines.

For the present calculation we consider two supercells containing 72 and 108 atoms (i.e. S_{72} and S_{108}) in order to test the convergence and the long-range effect of the coupled Al-Li substitution. A preliminary condition that tests the numerical accuracy and convergence of the results is that the undefective supercells of different sizes provide the same numerical result for the bulk properties (i.e. total energy per SiO_2 unit cell) (Lichanot et al., 1998). The total energies obtained with supercells containing 72 and 108 atoms are -440.0333 and -440.0298 Hartree per SiO_2 unit, respectively.

4.3.2 Paramagnetic defects $[AlO_4/Li^+]^+$ and $[AlO_4/Li]^q$

Three structural models for the lithium-compensated aluminium-hole centers were examined. Firstly we evaluated the model proposed by Mackey et al. (1970) for $[AlO_4/Li^+]^+$, supported by the results of the detailed EPR study of Howarth et al. (1997). Secondly we evaluated the two structural models proposed for the $[AlO_4/Li]^q$ center, placing the Li ion both in the center of the large channels that run parallel to c-axis and in the center of the small channels (see Fig. 4.1) as proposed by Walsby et al. (2003). After the introduction of the defect in the supercell, each structure was allowed to fully relax towards a minimal energy configuration.

$[AlO_4/Li^+]^+$

The proposed models of the $[AlO_4/Li^+]^+$ center (Mackey et al., 1970, Nuttall and Weil, 1981; Howarth et al., 1997) locate the hole on a short-bonded oxygen and position the Li compensator in the large channels, across from the hole-trapping oxygen and slightly displaced from the two fold axis position. For the evaluation of this model, we replaced Si' (cf. Fig. 4.1) with Al and a Li atom was placed in the center of the c-axis channel. A full relaxation of the structure was followed and the results are depicted in Fig. 4.2.

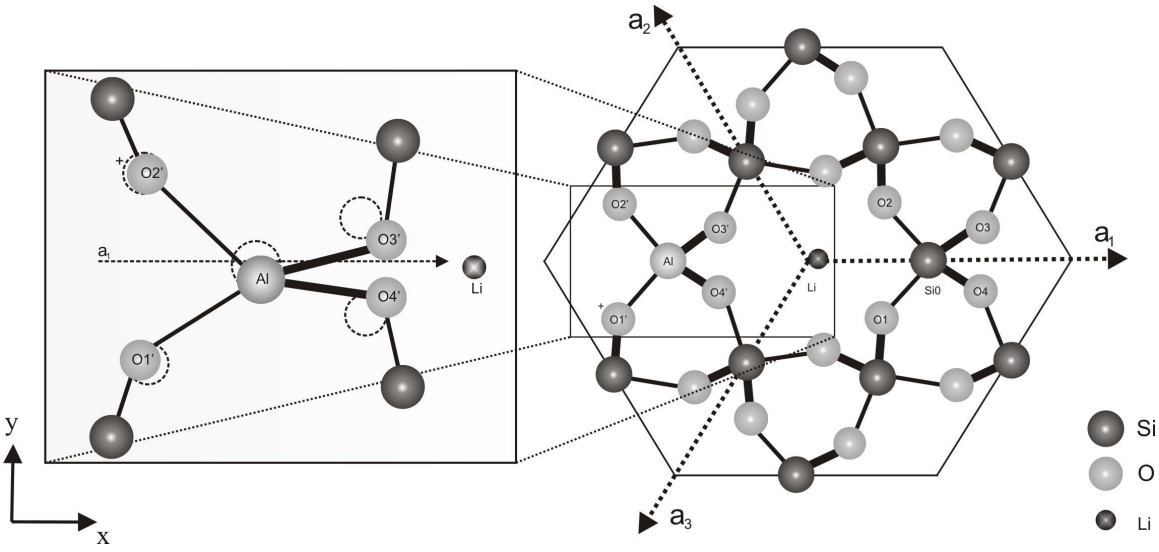

Figure 4.2: Structural model for $[AlO_4/Li^+]^+$ center. The $^+$ symbol denotes the position of the hole. Enlarged (left) the relaxed positions of the atoms are compared with the original Si and O positions of the ideal quartz structure (open circles). The original Li position was set at the center of the large c-axis channel.

The relaxation of the atoms surrounding the substitutional Al atom is significant. The Al-O(h^+) bond distance increases by ~22% compared to the normal Si-O bond. Table 4.1 lists the changes in bond distance that take place when Al replaces Si' and a Li atom is positioned at the center of one of the large c-axis channels. The fully relaxed structure has the Li ion both away from the center of the channel and slightly off the 2-fold symmetry axis (see Fig. 4.2 and Table 4.1) in agreement with the experimentally observed EPR spectra.

In this configuration, the Li^+ ion has a pseudo-tetrahedral coordination (Table 4.2). The calculated Li-O bond distances are significantly longer than those determined by Howarth et al. (1997) (i.e. Li-O4'=1.60 Å when using FITPKL and Li-O4'=1.73 Å

when using SCF-MO) but are now in agreements with experimental Li-O distances from X-ray diffraction experiments (e.g. Wenger and Armbruster, 1991).

Table 4.1: Calculated bond distances (Å) and spin densities of the $[AlO_4/Li(a_>)^+]^+$ defect

	$[AlO_4/Li(a_>)^+]^+$ in quartz					
	Bond distance (Å)			Spin population $(n_\alpha - n_\beta)$ (e)		
	S_{72}	S_{108}	MW		S_{72}	S_{108}
Al-O1'	1.730	1.725	1.663	O1'	0.015	0.018
Al-O2'	2.016	1.991	1.916	O2'	0.824	0.808
Al-O3'	1.791	1.786	1.717	O3'	0.005	0.006
Al-O4'	1.794	1.788	1.705	O4'	0.015	0.013
Li-O1	2.075	2.048		Al	-0.016	-0.016
Li-O2	2.113	2.078				
Li-O3'	2.053	2.032				
Li-O4'	2.050	2.028				
Li-O^*	3.499	3.556				
Li-O^*	3.604	3.590				

MW denotes data from Mombourquette and Weil (1985). O^* denotes the two additional oxygen atoms around the large c-axis channel (not labeled in Figure 4.1). All calculations made use of the B3LYP hybrid functional.

The localization of the hole in the case of the $[AlO_4/Li^+]^+$ was attained without any computational difficulties. Similar to the case of $[AlO_4]^0$ defect calculated by means of UHF by Laegsgaard end Stokbro (2001) the length of one Al-O bond (i.e. Al-O_2') increases significantly more than the other three Al-O bonds. As a result the spin

population is almost exclusively localized on this particular O atom that has been pushed away from Al (Table 4.1).

The principal values of the hyperfine interaction between the unpaired electron and the neighbouring ^{27}Al, ^{7}Li, ^{17}O nuclei have been calculated and the results are reported in Table 4.2. The calculated principal values of the hyperfine tensor (cf. A_x A_y A_z, cf Weil et al. 1994) are in relatively good agreement with the experimental values. The particularly good agreement obtained for the ^{17}O hyperfine suggests that the conventional B3LYP functional provides excellent results in terms of spin localisation for this particular situation.

Table 4.2: Comparison of experimental and calculated hyperfine constants of the $[AlO_4/Li(a_>)^+]^+$ (Gauss)

$[AlO_4/Li(a_>)^+]^+$	A	Exp	Calculated	
			S_{72}	S_{108}
	A_x	-8.08[b]	-4.78	-4.98
^{27}Al	A_y	-8.14[b]	-3.87	-4.88
(I=5/2)	A_z	-6.90[b]	-3.93	-4.02
	A_x	16.92[b]	3.95	3.63
^{17}O	A_y	14.85[b]	3.59	3.89
(I=5/2)	A_z	-110.78[b]	-110.06	-108.3
	A_x	-0.32[a]	0.28	0.26
^{7}Li	A_y	-0.24[a]	-0.16	-0.17
(I=3/2)	A_z	-0.28[a]	-0.21	-0.18

Experimental data from EPR measurements, [a]Nuttall and Weil 1981 and [b]Howarth et al. 1997.

$[AlO_4/Li]^q$

In the case of the $[AlO_4/Li]^q$ defect center we tested the stability of the two structural models proposed by Walsby et al. (2003).

- $[AlO_4/Li(a_<)^+]^+$

The first structural model that we investigated is similar to the model of $[AlO_4/Li(a_>)^+]^+$ but having Al substituting for Si0, and Li positioned in the center of the large c-axis channel, this time on the side of the short Si-O bonds (Fig.4.3). This structural model does not require any change in the charge of the Li ion, and therefore we are going to simply denote it $[AlO_4/Li(a_<)^+]^+$ and abandon the notation proposed by Walsby et al. (2003). After the complete relaxation of the structure we obtained a structural arrangement similar to the case of $[AlO_4/Li(a_>)^+]^+$ but with the hole trapped on one of the long-bonded O, across from the Li compensator (Fig.4.3 and Table 4.3).

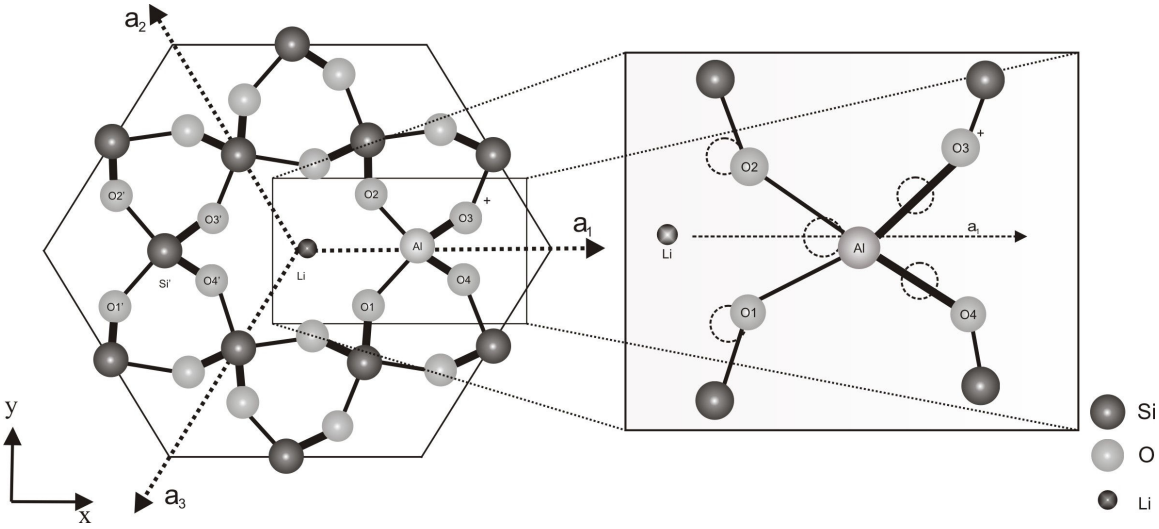

Figure 4.3: Structural model for $[AlO_4/Li(a_<)^+]^+$ center. The $^+$ symbol denotes the position of the hole. Enlarged (left) the relaxed positions of the atoms are compared with the original Si and O positions of the ideal quartz structure (open circles). The original Li position was set at the center of the large c-axis channel.

As noted in Table 4.3 and Fig. 4.3, significant displacements of the atoms surrounding the substitutional Al are taking place. The Al atom departs from 2-fold symmetry axis previously occupied by Si0. Important changes in the Al-O bond distances compared to the ideal quartz structure can be noted, with the largest displacement noted for O3 atom, on which the hole is located. The Al-O3 bond distance increases by ~20% compared to the ideal Si-O3 bond.

Table 4.3: Calculated bond distances (Å) and spin densities for the $[AlO_4/Li(a_<)^+]^+$ defect

	$[AlO_4/Li(a_<)^+]^+$ in quartz				
	Bond distance (Å)		Spin population (n_α-n_β) (*e*)		
	S_{72}	S_{108}		S_{72}	S_{108}
Al-O1	1.794	1.743	O1	0.013	0.061
Al-O2	1.793	1.804	O2	0.005	0.003
Al-O3	2.017	1.983	O3	0.824	0.803
Al-O4	1.731	1.740	O4	0.015	0.017
Li-O1	2.050	1.979	Al	-0.016	-0.020
Li-O2	2.050	2.075			
Li-O3’	2.071	2.065			
Li-O4’	2.112	2.126			
Li-O*	3.613	3.662			
Li-O*	3.573	3.592			

O* denotes the two additional oxygen atoms around the large c-axis channel (not labeled in Figure 4.1). All calculations were done using the B3LYP hybrid functional.

The calculated principal values of the hyperfine constants are again comparable with the experimental values obtained by Walsby et al. (2003) (Table 4.4). The very good

agreement obtained between the calculated and the experimental values for the ^{7}Li hyperfine suggest a Li-O(h^{+}) distance extremely closed to the experimentally observed one. The Li-O(h^{+}) distance calculated by Walsby et al. (2003) assuming a spin density between 0.64 and 1.0, is reported to range from 3.4 to 3.9 Å. The present calculation resulted in a ^{7}Li-O(h^{+}) distance of 3.936 Å.

Table 4.4: Comparison of experimental and calculated hyperfine constants of the $[AlO_4/Li(a_<)^{+}]^{+}$ (Gauss)

$[AlO_4/Li(a_>)^{+}]^{+}$	A	Exp	Calculated	
			S_{72}	S_{108}
^{27}Al (I=5/2)	A_x	-6.395	-3.89	-4.78
	A_y	-7.483	-4.74	-5.54
	A_z	-7.507	-4.89	-5.65
^{17}Li (I=3/2)	A_x	-0.322	-0.205	-0.076
	A_y	-0.195	-0.162	-0.083
	A_z	0.232	0.277	0.137
^{17}O (I=5/2)	A_x	-	-5.15	3.83
	A_y	-	-6.21	3.53
	A_z	-	-104.00	-107.4

The experimental values are the ones reported for the $[AlO_4/Li]^{q}$ center by Walsby et al. (2003).

- $[AlO_4/Li(c_{small})^+]^+$

For the second model the Li atom was placed in the center of one of the small channels (Fig. 4.1) and Al replaced one nearby Si atom. For simplicity we will denote this model $[AlO_4/Li(c_{small})^+]^+$, where c_{small} denotes the approximate location of the Li atom in one of the small channels running parallel to c-axis. After the introduction of the defect in the supercell, the structure was allowed to fully relax towards a minimum energy configuration. The resulting geometry is depicted in Fig. 4.4. Following relaxation, the Li atom moves from the center of the small channel towards one of its sides. It is important to note here that the small and large quartz channels (i.e. as viewed from the (0001) direction) have in fact a helicoidal structure thus allowing for positions other than the center of the channels to be sufficiently large to accommodate small cation impurities.

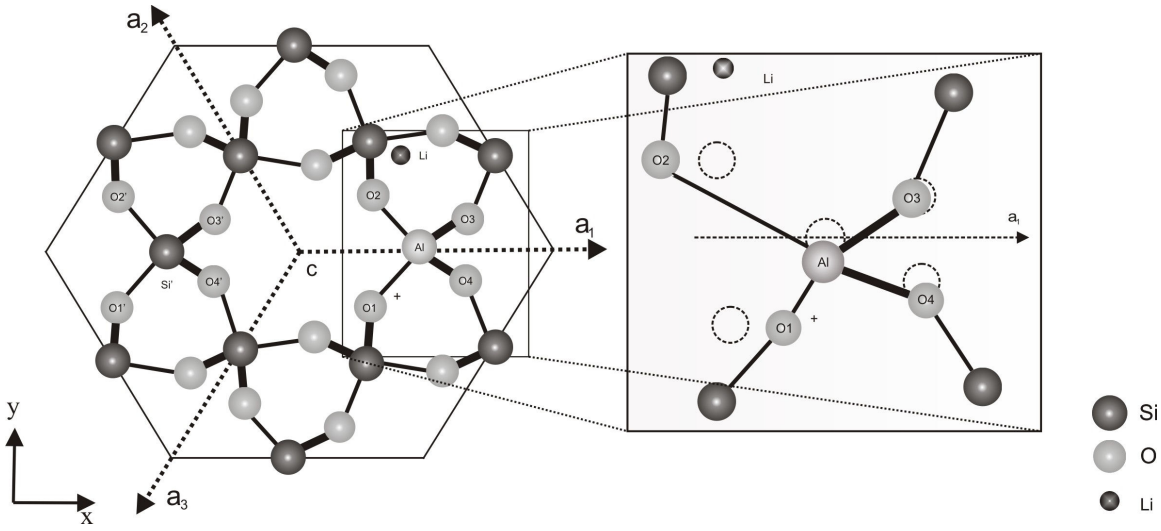

Figure 4.4: Structural model for $[AlO_4/Li(c_{small})^+]^+$ center. The $^+$ symbol denotes the position of the hole. Enlarged (right) the relaxed positions of the atoms are compared with the original Si and O positions of the ideal quartz structure (open circles). The original Li position was set at the center of the small channel running parallel to c-axis.

Following the complete relaxation of the structure, the distortion of the [AlO_4] tetrahedron is significant (Table 4.5 and Fig.4.5). The Al atom is displaced from the 2-fold axis of symmetry and the largest change in position (Table 4.5) is experienced by the hole-trapping O atom (i.e. O1). The hole-trapping atom, O1 is however a short bonded O atom. Therefore, this structural model differs significantly from the model proposed by Walsby et al. (2003) for $[AlO_4/Li^+]^q$, which locates the hole on a long-bonded O atom.

Table 4.5: Calculated bond distances (Å) and spin densities for the $[AlO_4/Li(a_<)^+]^+$ defect

	$[AlO_4/Li(a_<)^+]^+$ in quartz		
	Bond distance (Å)	Spin population (n_α-n_β) (*e*)	
	S_{72}		S_{72}
Al-O1	2.015	O1	0.825
Al-O2	1.793	O2	0.010
Al-O3	1.781	O3	0.020
Al-O4	1.728	O4	0.012
Li-O2	1.996	Al	-0.017
Li-O3	2.174		
Li-O^{**}	2.428		

O^{**} denotes the oxygen atom (not labeled in Figure 4.4) located on the other side of the small channel. All calculations were done using the B3LYP hybrid functional.

The calculated Li-O bond distances are again in very good agreement with the Li-O bonds determined from X-ray diffraction measurements (e.g. Wenger and Armbruster, 1991). The calculated principal values of the ^{27}Al and ^{7}Li hyperfine constants (Table 4.6)

are close to those reported for $[AlO_4/Li^+]^+$ (Nuttall et al., 1981; Howarth et al., 1997) and $[AlO_4/Li]^q$ centers (Walsby et al., 2003) with significant differences noted only in the case of ^{17}O hyperfine structure.

Table 4.6: Comparison of experimental and calculated hyperfine constants of the $[AlO_4/Li(a_<)^+]^+$ (Gauss)

$[AlO_4/Li(c_{small})^+]^+$	A	Exp	Calculated
			S_{72}
^{27}Al (I=5/2)	A_x	-6.395	-3.79
	A_y	-7.483	-4.70
	A_z	-7.507	-4.78
^{17}Li (I=3/2)	A_x	-0.322	0.38
	A_y	-0.195	-0.19
	A_z	0.232	-0.25
^{17}O (I=5/2)	A_x	-	-73.15
	A_y	-	-111.45
	A_z	-	3.88

The experimental values are the ones reported for the $[AlO_4/Li]^q$ center by Walsby et al. (2003).

4.4. Discussions and conclusion

Two types of Li compensated Al-associated centers have been proposed to exist in quartz based on experimental EPR studies (Nuttall and Weil, 1981; Howarth et al., 1997; Walsby et al., 2003) The fundamental distinction between the two types of centers lies in the location of the trapped hole; short-bonded vs. long-bonded O atom.

The first structural model proposed proposed by Nuttall and Weil (1981), locates the Li atom close to the center of the large channels running parallel to c-axis, and the hole on a short-bonded O atom. The structural model derived by Nutall and Weil was based solely on the magnitudes and directions of the ^{27}Al and ^{7}Li hyperfine constants. Although two possible positions were determined for the location of Li, only the position close to the center of the c-axis channel was considered reasonable. The second Li position was dismissed because it would have placed Li too close to one O atom. However, our present calculations show that a significant distortion of the AlO_4 tetrahedron allows Li to be positioned close to one side of the small channels. As a result two structural models (i.e. $[AlO_4/Li(a_>)^+]^+$ and $[AlO_4/Li(c_{small})^+]^+$) both having the unpaired electron located on short-bonded O are possible (Fig 4.2 and Fig. 4.4). Nevertheless, the similarities between the ^{27}Al and ^{7}Li hyperfine constants belonging to these centers (Table 4.3 and Table 4.6) would make their distinction based solely on these parameters impossible. The calculated ^{17}O hyperfine structures, on the other hand, are sufficiently different and represent the only modality to distinguish these two structural models (Table 4.3 and Table 4.6). The values obtained by Howarth et al. (1997) for the ^{17}O hyperfine matrix are in good agreement with our calculated values (Table 4.3) confirming the structure of the $[AlO_4/Li(a_>)^+]^+$ model. This, however, does not dismiss the possibility of a second structural model with similar ^{27}Al and ^{7}Li hyperfine constants and a distinct ^{17}O hyperfine structure (Table 4.6).

The second structural model proposed on the basis of experimental findings (Walsby et al. 2003) suggests the location of the hole to be on a long-bonded O atom. Similar to the approach used by Nuttall and Weil (1981), Walsby et al. determined the

location of the Li atom using the magnitude and orientation of the ^{7}Li hyperfine constants. Nonetheless, this approach resulted in two possible positions for Li: i) a site close to the center of the large channel and ii) a site close to the edge of the small channel. Walsby et al. (2003) cautioned that the second location would result in a rather small Li-O distance (i.e. 1.4-1.8 Å, considering a spin density of 0.8-1.0). The present theoretical calculation, evaluates the structural model proposed by Walsby et al. considering the two possible Li positions but only the $[AlO_4/Li(a_<)^+]^+$ preserved the distinctive characteristics of the center proposed by Walsby et al. (i.e. unpaired electron located on the long-bonded O atom). When placing the Li in the small channels, a short-bonded O is preferred for hole trapping (Fig.4.4). Therefore we can conclude that the defect center experimentally observed by Walsby et al. (2003) is an $[AlO_4/Li(a_<)^+]^+$ center, with Li located close to the center of the large c-axis channel and across from a long-bonded O atom that traps the hole (Fig. 4.3).

An explanation for the existence of two distinct types of aluminum lithium oxygenic-hole center, suggested by Walsby et al. (2003), was the possibility of compensation with an alkalide anion Li^-, similar to the well known Na^- and K^- ions (Dye and DeBacker, 1987). However our theoretical calculations suggest that Li^+ is the charge compensator regardless of the location of the trapped hole (i.e. long-bonded or short bonded O atoms), in agreement with the results of Brazzelli et al. (2004) who concluded that Li^- ion in silica is unstable.

The explanation that we suggest for the presence of two distinct type of Li compensated Al hole centers (i.e. distinction made solely on the location of the trapped hole) is directly linked to the diffusion mechanism of Li in quartz. If we assume that Al is

randomly incorporated into the quartz structure, the diffusion of Li^+ through the large channels running parallel to the c-axis would result in two different structural configurations: i) Li on the $a_>$ side and ii) Li on the $a_<$ side, with respect to Al. Upon irradiation these diamagnetic structure will trap a hole on one O atoms belonging to the AlO_4 tetrahedron and located on the opposite side of the Li atom. Therefore depending on the location of the Li charge compensator, this would give rise to the two distinct types of Al-Li defect centers.

Considering that in fact, three type of locations are possible for Li (i.e. $[AlO_4/Li^+(a_<)]^0$, $[AlO_4/Li^+(a_>)]^0$ and $[AlO_4/Li^+(s_{small})]^0$) with two of them resulting in a center that traps the hole on a short-bonded O atom, it is not surprising the prevalent observation of this particular type of Li compensated center. Also, important to note is that theoretical calculation comparing the ground state energy of $[AlO_4/Li^+(a_<)]^0$ and $[AlO_4/Li^+(a_>)]^0$ diamagnetic precursors (see Chapter 3) showed that $[AlO_4/Li^+(a_<)]^0$ is more stable than its counterpart and therefore $[AlO_4/Li^+(a_>)]^+$ would be energetically easier to produce.

It would be very interesting to compare between the ground state energies of the three possible Li compensated Al-associated paramagnetic centers but due to the effective charge that exists on these centers, a comparison between their total energies would not be physically meaningful (Dovesi et al. 2006).

The calculated ^7Li and ^{17}O hyperfine constants are in good agreement with experimental values, while consistent discrepancies are apparent between the calculated and experimental ^{27}Al hyperfine constants. Several Al basis sets have been tested but there was no significant improvement of the results.

4.5 References

Brazzelli S, Di Valentin C, Pacchioni G (2004) Comparative ab initio study of the structure and stability of H^- and Li^- anions in silica networks. Physical Review B 69: 024101

Continenza A, Di Pomponia A (1996) All-electron study of the electronic properties of quartz with Al substitutional impurity. Physical Review B 54:13687

Cora, F. and Pisani, C. (1994) A quantum-mechanical *ab-initio* simulation of neutral and charged point-defects in alpha-quartz. Modelling and Simulation in Material Science and Engineering, 2: 965-974

Dickson RS and Weil JA (1990) The magnetic properties of the oxygen-hole aluminum centers in crystalline SiO_2. Canadian Journal of Physics 68: 630-642

Dovesi R, Saunders VR, Roetti C, Orlando R, Zicovich-Wilson CM, Pascale F Civalleri B, Doll K, Harrison NM, Bush IJ, D'Arco P, Llunnell M (2006) CRYSTAL2006, User's Manual; http://www.crystal.unito.it, University of Torino, Torino

Dye JL, DeBacker MG (1987) Physical and chemical properties of alkalides and electrides. Annual Reviews of Physical Chemistry 38: 271-301

Frondel G (1962) Dana's system of mineralogy. 7th ed. Wiley, Ney York, NY.

Howarth DF, Mambourquette MJ, Weil JA (1997) The magnetic properties of the oxygen-hole aluminum centers in crystalline SiO_2. V. ^{17}O-enriched $[AlO_4/Li^+]^+$ and dynamics thereof. Canadian Journal of Physics 75: 99-115

Laegsgaard J, Stokbro K (2001) Hole trapping at Al impurities in silica: a challenge for density functional theories. Physical Review Letters 86: 2834-2837

Lee C, Yang W, Parr RG (1988) Development of the Colle-Salvetti correlation-energy formula into a functional of the electron density, Physical Review B 37: 785-789

LePage Y, Calvert LD, Gabe EJ (1980) Parameter variation in low quartz between 94 and 298 K. Journal of Physics and Chemistry of Solids, 41: 721-72

Lichanot A., Larrieu C., Orlando R., Dovesi R. (1998) Lithium trapped-hole centre in magnesium oxide. An ab initio supercell study. Journal of Physics and Chemistry of Solids 59: 7-12

Mackey JH (1963) EPR study of impurity-related color centers in germanium-doped quartz. Journal of Chemical Physics 39: 74-83.

Mackey JH, Boss JW, Wood DE (1970) EPR study of substitutional-aluminum-related hole centers in synthetic alpha-quartz. Journal of Magnetic Resonance 3: 44-54

Mombourquette MJ, Weil JA, Mezey PG (1984) An initio SCF-MO calculations on AlO_4 centers in alpha-quartz. I. Canadian Journal of Physics 62: 21-34

Mombourquette MJ, Weil JA (1985) Ab initio self-consistent molecular-orbital calculations on AlO_4 centers in alpha-quartz. II. Canadian Journal of Physics 63: 1282-1293

Mombourquette MJ, Weil JA (1986) Structure determination of the AlO_4 hole centers in α-quartz by EPR and SCF MO. Journal of Magnetic Resonance 66: 105-117

Merawa M, Labeguerie P, Ugliengo P, Doll K, Dovesi R (2004) The structural, electronic and vibrational properties of LiOH and NaOH: an ab initio study. Chemical Physics Letters 387: 453-459

Monkhorst HJ, Pack JD (1976) Special points for Brillouin-zone integrations. Physical Reviews B 13: 5188-5192

Montanari B, Civalleri B, Zicovich-Wilson CM, Dovesi R (2006) Influence of the exchange-correlation functional in all-electron calculations of the vibrational frequencies of corundum (alpha-Al2O3), International Journal of Quantum Chemistry 106: 1703-1714

Nada R., Catlow CRA, Dovesi R and Pisani C (1990) An Ab-Initio Hartree-Fock Study of alpha-Quartz and Stishovitei Physics and Chemistry of Minerals 17: 353-362

Nuttall RHD and Weil JA (1981) The magnetic properties of the oxygen-hole aluminum centers in crystalline SiO_2.II. $[AlO_4/H^+]^+$ and $[AlO_4/Li^+]^+$. Canadian Journal of Physics 59: 1709-1718

Pacchioni G, Frigoli F, Ricci D, Weil JA (2001) Theoretical description of hole localization in a quartz Al center: The importance of exact electron exchange. Physical Review B, 63: 054102

Sicolo S, Palma G, Di Valentin C, Pacchioni G (2007) Structure and ESR properties of self-trapped holes in pure silica from first-principles density functional calculation, Physical Review B 76:075121

Sim F, Catlow CRA, Dupuis M, Watts JD (1991) Ab initio self-consistent molecular-orbital on defects associated with radiation-damage in alpha-quartz. Journal of Chemical Physics 95: 4215-4224

To J, Sokol AA, French SA (2005) Hole locatization in $[AlO_4]$ defects in silica materials. Journal of Chemical Physics 122:144704

Walsby CJ, Less NS, Claridge RFC, Weil JA (2003) The magnetic properties of oxygen-hole aluminum centers in crystalline SiO_2. VI. A stable AlO_4/Li center. Canadian Journal of Physics 81: 583-597

Weil JA (1984) A review of electron spin resonance and its applications to the study of paramagnetic defects in quartz. Physics and Chemistry of Minerals 10:149-165

Weil J, Bolton JR, Wertz JE (1994) Electron paramagnetic resonance: elementary theory and practical applications, Wiley-Interscience, New York

Weil JA (2000) A demi-century of magnetic defects in α-quartz. In: Pacchioni G, Skuja L, Griscom DL eds., Defects in SiO_2 and related dielectrics: Sciences and Technology. Kluer Academic, Netherlands, 197-212

Wenger, M. and Armbruster, T. (1991) Crystal chemistry of lithium: oxygen coordination and bonding. European Journal of Mineralogy, 3: 387-399

Chapter 5

Theoretical modeling of the Al paramagnetic center and its precursors in stishovite

Previous electron paramagnetic resonance (EPR) spectroscopic study of gamma-ray-irradiated stishovite at 77K detected an Al hole center, which was proposed to be an $[O_2^{3-}\text{-}Al^{3+}]$ defect. First-principle quantum-mechanical calculations show that the unpaired spin is 85% localised on one of the six oxygen atoms at an AlO_6 octahedron, while the calculated ^{27}Al hyperfine constants are similar to those determined by EPR experiments. Theoretical results allow us to propose the Al center to represent an $[AlO_6]^0$ defect, and hole hopping among equivalent oxygen atoms is responsible for its detection only at cryogenic temperatures. Theoretical calculations also show that diamagnetic precursors $[AlO_6/H^+]^0$, $[AlO_6/Li^+]^0$ and $[AlO_6/Na^+]^0$ are stable in stishovite. The calculated OH bond distance and orientation are in excellent agreement with those inferred from FTIR spectra and previous theoretical calculations. The calculated $[AlO_6/Li^+]^0$ and $[AlO_6/Na^+]^0$ defects suggest that monovalent cations such as Li^+ and Na^+ are potentially important in accommodating Al in stishovite in the lower mantle.

5.1 Introduction

Radiation-induced defects (RIDs) in high-pressure SiO_2 polymorphs, coesite and stishovite, have attracted considerable interests because of their potential applications for dating meteor impact events (Ikeya, 1993). Electron paramagnetic resonance (EPR) spectroscopic studies of artificially irradiated stishovite have detected an E' center, an oxygen hole center, an Al hole center, an atomic hydrogen center and a Ti center (Devine and Hubner, 1989; Ogoh et al., 1994; 1995; 1996 a,b; Tani, 2000; Tani et al., 2000). Of these, the Al hole center has anisotropic g-factor values (g_x = 2.0155, g_y = 2.0094, and g_z = 2.0033) and a characteristic ^{27}Al hyperfine structure (A_x = 0.394 mT, A_y = 0.372 mT, and A_z = 0.436 mT). These g-factor values and the hyperfine structure have lead Ogoh et al. (1996a) to suggest this defect to be an O_2^{3-} type center linked to an Al^{3+} ion substituting for Si^{4+} (i.e., [O_2^{3-}-Al^{3+}]). Nilges et al. (2008) reviewed the proposed O_2^{3-} type centers in the literature and cautioned that they cannot be positively identified on the basis of g-factor values alone, because several other oxygen centers such as O^- and O_2^- are known to have similar g-factor values. Recently, we performed *ab initio* calculations for the best-studied O_2^{3-} centers in CaF_2 and SrF_2 (Botis et al., 2009), for which their ^{17}O hyperfine constants have been determined by use of ^{17}O-enriched crystals (Bill, 1969; see also Schweizer and Spaeth, 1999). Our theoretical calculations showed that these centers in CaF_2 and SrF_2 do have an equal distribution of the unpaired spin on two substitutional oxygen atoms separated by a distance of 2.47 Å, hence a first confirmation of the O_2^{3-} type centers.

This contribution is a continuation of our effort on the O_2^{3-} type centers (Botis et al. 2009) and investigates the Al hole center in stishovite (Ogoh et al., 1996a) by *ab-initio*

calculations at the density functional theory (DFT) level. This investigation was motivated by not only a need to better understand the Al hole center in stishovite but also our interests in its possible diamagnetic precursors, which are expected to involve H^+ and other monovalent charge compensators. Recent experimental studies have demonstrated that stishovite is a potential host for accommodating significant amounts of Al and H, which are expected to have profound influences on the stability and properties of this important phase in the lower mantle (Pawley et al., 1993; Chung and Kagi, 2002; Panero et al., 2003). There have been a number of recent experimental and theoretical studies on the incorporation of Al and H in stishovite (Oganov and Brodholt, 2000; Ross et al., 2003; Gibbs et al., 2004; Panero and Stixrude, 2004; Bromiley et al., 2006; Panero, 2006; Stebbins et al., 2006; Lakshtanov et al., 2007; Litasov et al., 2007). Our theoretical results for the Al hole center and its diamagnetic precursors are expected to shed new lights into mechanisms for the incorporation of Al and H in stishovite.

5.2 Computational methodology

All calculations were performed with the CRYSTAL06 code, which computes the electronic structures and properties of periodic systems by use of the Hartree-Fock (HF), DFT and various hybrid approximations (Dovesi et al., 2006) using Gaussian-type functions (GTF) localised at atoms as the basis set for the expansion of the crystalline orbitals.

The basis sets used for Si and O were those reported by Nada et al. (1990). The basis sets used for Al, H, Li and Na were the ones reported by Montanari et al. (2006), Dovesi et al. (1983), Merawa et al. (2004) and Dovesi et al. (1991), respectively.

The exchange-correlation contribution is the result of a numerical integration of the electron density and its gradient performed over a grid of points. In order to obtain high accuracy energy calculation and geometry optimization a pruned grid consisting of 75 radial points and 434 angular points was used (LGRID). The high accuracy grid is recommended for high accuracy energy calculations and geometry optimisation (Dovesi et al., 2006).

The supercell model was used for the calculation of the Al defect center. This procedure consists of building a supercell of the host crystal, which includes a multiple of the original unit cell so that the system maintains its periodicity. However, the size of the supercell must be so chosen to minimize possible defect-defect interactions. For this purpose the convergence of all defect related properties (i.e. spin density, hyperfine coupling constants) must be evaluated with respect to the supercell size. The effect of the supercell size (i.e. 49 and 96 atoms or S_{48} and S_{96}) was carefully checked, and after several tests we concluded that a 48-atom supercell was sufficiently large to correctly reproduce the experimentally measured properties of the Al defect. However, for the calculation of the precursors of the Al center we employed 96-atom supercells.

The reciprocal space integration was performed by sampling the Brillouin zone of the unit cell with the 8*8*8 Pack-Monkhorst net (for calculations of the bulk structure) and a 4*4*4 Pack-Monkhorst net (for calculations employing a 48 atoms and 96 atoms supercell) (Monkhorst and Pack, 1976).

The choice of functionals is crucial especially for the calculation of magnetic properties (i.e. hyperfine tensors). In this context the performance of a functional is evaluated strictly on the basis of its ability to provide good spin densities not on average

but at the nuclear position. Analogous with the complex situation of the $[AlO_4]^0$ defect center in quartz, special attention must be paid to the choice of the functional used for the study of hole-type defect centers in insulators (Pacchioni et al., 2001; To et al., 2005; Sicolo et al., 2007). While a pure DFT approach fails to describe the localised behaviour of the unpaired electron in the defect, HF methods produce solutions where spins are too localised. Nevertheless, the use of DFT approximation is preferred over the unrestricted Hartree-Fock (UHF) method because of its higher accuracy in determining properties such as bond dissociation and the energy of reactions (To et al., 2005).This problem can be avoided by using hybrid functionals in which a mixture of HF exchange and DF exchange correlation is present, with special care to the percentage of hybrid mixing (Sicolo et al., 2007). From this point of view CRYSTAL06 proves to be an excellent computational tool, allowing mixing of the HF and DFT exchange functionals to any desired degree. We have constructed a series of hybrid functionals using a scheme similar to the one employed by Alfredsson et al. (2005). The generic hybrid functional (i.e. $F_\alpha B_{100-\alpha}LYP$) with an α % of HF exchange was mixed with (100-α) % Becke (Becke, 1988) exchange and Lee-Yang-Par (Lee et al., 1988) correlation. The variation of the hybrid mixing parameter α while monitoring the calculated electronic properties that are known to strongly depend on the choice of the functional (i.e. spin density) allows the selection of the best α value that can reproduce the experimental results.

5.3 Results

5.3.1 Bulk structure of stishovite

Stishovite, the only octahedrally coordinated SiO_2, has attracted considerable amounts of interest due to both its intrinsic properties and its possible role as a model for more complex compounds with the same Si coordination (e.g. majorite garnet, hollandite and perovskite). Consequently, the electronic structure and stability of stishovite have been the subjects of several previous theoretical studies (Alvarez and Rez, 1998; Nada et al., 1990; Keskar et al. 1991; Jolly et al. 1994; Ottonello et al., 2009).

Stishovite belongs to the $P4_2/mnm$ space group with a structure consisting of SiO_6 octahedra that share edges along the *c* axis and corners in the *ab* plane (Fig. 5.1a). The edge sharing octahedra having two types of Si-O bonds (i.e. equatorial Si-O bonds of 1.755 Å, and apical Si-O bonds of 1.811 Å; Yamanaka et al. 2002) form pillars along the *c*-axis, separated by empty channels (Fig. 5.1b).

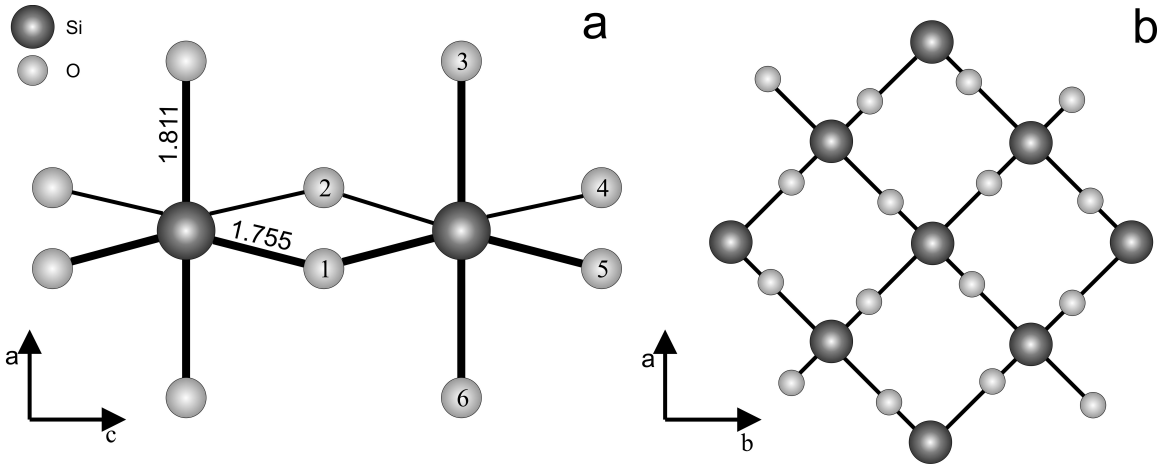

Figure 5.1: Structure of stishovite ($P4_2/mnm$) projected on the a) (010) plane and b) (001) plane.

The lattice parameters and fractional coordinates have been optimised using the B3LYP functional and three additional hybrid functionals with different % of HF exchange, and the equilibrium geometries have been obtained by a full relaxation of the structure in each case (Table 5.1). The discrepancies between the experimentally determined (Yamanaka et al. 2002) and the calculated structural parameters in all cases are less than 1.3 %.

Table 5.1. Comparison between the calculated and experimental unit cell parameters and Si-O distance for stishovite

	B3LYP	$F_{25}B_{75}$LYP	$F_{30}B_{70}$LYP	$F_{35}B_{65}$LYP	Experimental[a]
a (Å)	2.702	2.698	2.693	2.688	2.666
c (Å)	4.221	4.213	4.203	4.195	4.181
c/a	1.568	1.561	1.560	1.560	1.560
Si-O1,2,4,5	1.778	1.775	1.772	1.769	1.757
Si-O3,6	1.829	1.825	1.821	1.817	1.811

[a] Experimental values as determined from x-ray diffraction data (Yamanaka et al. 2002).

5.3.2 Geometry, electronic structure and hyperfine constants of the Al center

Following geometry optimisation of pure stishovite, and the construction of a 48-atoms supercell, a substitutional Al atom was added to the centre of the supercell (Fig. 5.2). This was followed by relaxation of the entire structure towards a minimum energy configuration.

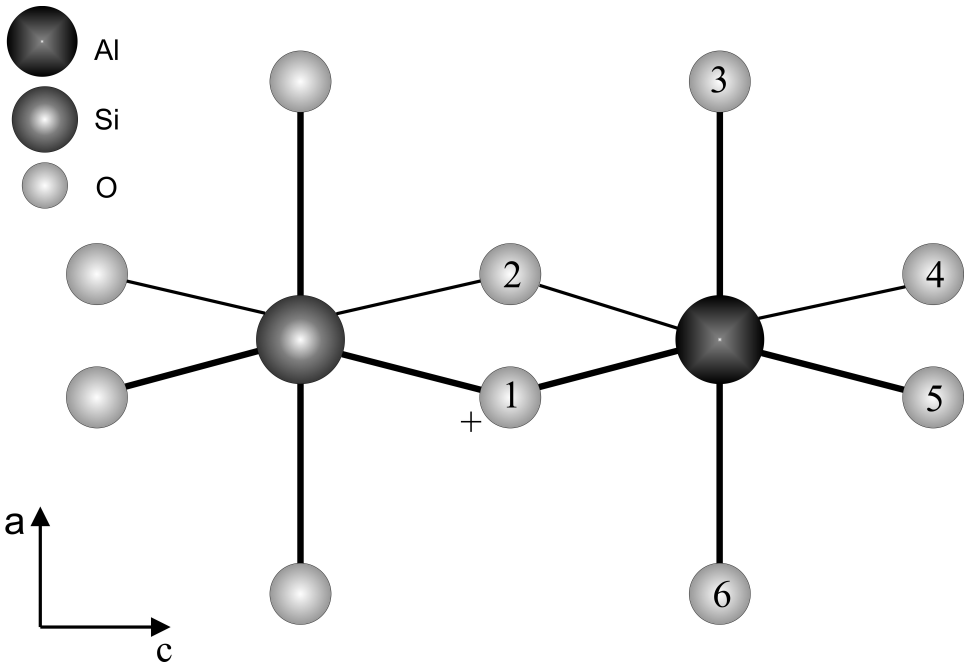

Figure 5.2: New model for the Al hole center in stishovite.

The results obtained by using the B3LYP functional (Table 5.2) show that the calculation of the electronic properties of the Al hole center in stishovite presents the same challenges as previously reported for the $[AlO_4]^0$ defect in quartz, specifically a very weak localisation of the unpaired electron.

Despite the poor localisation of the hole, the electronic structure of the defect suggests it has an O^--type structure rather than the O_2^{3-} model proposed by Ogoh et al. (1996a). Moreover, with increasing HF mixing (Table 5.2) the localisation of the hole is attained, with values up to 85% spin density on one of the O atoms around the octahedrally coordinated Al. Therefore, we can conclude that the substitution of Si^{4+} by Al^{3+} in stishovite followed by hole trapping results in a $[AlO_6]^0$ paramagnetic defect, in which the unpaired electron is almost exclusively localised on one O atom.

Table 5.2. Calculated spin population (*e*) and bond distances for the Al hole center in stishovite

	B3LYP	$F_{25}B_{75}$LYP	$F_{30}B_{70}$ LYP	$F_{35}B_{65}$LYP
		Spin density (n_α-n_β) (*e*)		
Al	-0.015	-0.016	-0.016	-0.015
O1	0.402	0.682	0.794	0.856
O2	0.056	0.022	0.011	0.007
O3	0.040	0.032	0.025	0.020
O4	0.012	0.001	0.006	0.001
O5	0.074	0.020	0.000	0.000
O6	0.040	0.032	0.025	0.020
Si	-0.023	-0.021	-0.020	-0.019
		Bond distance (Å)		
Al-O1	1.886	1.910	1.918	1.919
Al-O2	1.835	1.829	1.824	1.822
Al-O3	1.892	1.882	1.875	1.870
Al-O4	1.823	1.805	1.797	1.849
Al-O5	1.857	1.852	1.851	1.791
Al-O6	1.892	1.882	1.875	1.870

Labels of atoms are the same as those in Figure 5.2.

As expected, full relaxation of the structure with the Al center results in larger Al-O bond distances (Table 5.3) than the original Si-O bonds. Particularly, the Al-O1 bond distance involving the hole-trapping O atom increases with increasing hole localisation (Table 5.2) to values of ~7 % larger than the original Si-O bond distance. It is interesting to note that the relaxation of the structure has a local character being limited to the AlO_6 octahedron, with minimal (i.e. 0.002 Å) to no effect on the second bonding-sphere atoms.

Table 5.3: Comparison of experimental and calculated hyperfine constants (Gauss)

	A	Exp[a]	B3LYP	$F_{25}B_{75}$LYP	$F_{30}B_{70}$ LYP	$F_{35}B_{65}$LYP
	A_x	3.94	-4.14	-4.58	-4.68	-4.74
^{27}Al	A_y	3.72	-3.57	-3.64	-3.58	-3.57
(I=5/2)	A_z	4.36	-4.27	-4.58	-4.81	-4.89
	A_x	-	-58.4	-97.5	-94.3	-121
^{17}O	A_y	-	1.73	2.49	3.05	1.87
(I=5/2)	A_z	-	1.54	2.19	2.76	1.5
	A_x	-	4.76	4.88	4.76	4.63
^{29}Si	A_y	-	4.96	4.68	4.95	4.40
(I=1/2)	A_z	-	4.53	4.33	4.41	3.97

[a] Experimental data from powder EPR measurements, Ogoh et al. 1996a. Note that EPR experiments cannot determine the sign of the hyperfine constants.

The principal values of the hyperfine tensors (A_x, A_y and A_z), which provide a measure of the interaction between the unpaired electron and the nuclear spin, were calculated for ^{27}Al, ^{17}O and ^{29}Si, and compared with results obtained from powder EPR measurements (Table 5.3). The calculated ^{27}Al hyperfine constants are in general agreement with experimental values. Particularly, the calculated spin on the Al atom is negative, which is similar to that suggested for the $[AlO_4]^0$ center in quartz (Barker, 1975) and is partly responsible for the small ^{27}Al hyperfine constants (Table 5.3). We caution that the ^{27}Al hyperfine constants alone can not provide any information about the hole localization because similar values of the ^{27}Al hyperfine interaction have been obtained for spin densities from 40 to 85% (Table 5.3). The most definitive experimental tool for distinguishing the O^- and O_2^{3-} -type centers is the ^{17}O hyperfine structure (i.e. interaction involving a single or two equivalent oxygen atoms). Unfortunately, ^{17}O

hyperfine structure was not resolved in the EPR experiment of Ogoh et al. (1996a), owing to the fact that the natural isotope abundance of ^{17}O (I=5/2) is only 0.038%. Similarly, the expected ^{29}Si hyperfine structure (i.e. interaction with one nearest Si nucleus irrespective of the O^- or O_2^{3-} models) was not disclosed in EPR spectra either, owing to the low natural abundance of ^{29}Si (4.67%). The calculated ^{17}O and ^{29}Si hyperfine values (Table 5.3) may be tested by future EPR measurements.

5.3.3 $[AlO_6/M^+]^0$ precursors

The similarities between the Al hole center in stishovite and the $[AlO_4]^0$ center in quartz suggest the possibility of similar types of diamagnetic precursors. EPR experiments have shown that the $[AlO_4]^0$ center in quartz formed from diamagnetic defects of the type $[AlO_4/M^+]^0$, where M=H, Li, Na and K (Mackey, 1963; Mackey et al., 1970; Nuttall and Weil, 1981; Dickson and Weil, 1990; Howarth et al., 1997; Mombourquette and Weil, 1985; Cora and Pisani, 1994; Botis and Pan, 2009). Therefore, we investigated several charge compensation mechanisms for the Al incorporation in stishovite, in which monovalent alkali ions (i.e. M= Li and Na) serve as charge compensators, to $[AlO_6/M^+]^0$ type structures, in addition to the well studied $[AlO_6/H^+]^0$ (Ross et al., 2003).

Our calculations for these diamagnetic defects were started by inserting the compensating ion to the center of one of the stishovite channels, next to a substitutional Al (Fig. 5.1b). The resulting structures were then allowed to fully relax towards minimum energy configurations. Particularly, our calculations of these diamagnetic precursors utilised 96-atom supercells in order to minimize possible defect-defect interactions and provide an accurate picture of the structural relaxation around the defect. The relaxed

geometries of the $[AlO_6/M^+]^0$ diamagnetic defects are shown in Figure 5.3. In the case of $[AlO_6/H^+]^0$ relaxation of the stishovite structure to accommodate the defect is very small. The H atom moves from the center of the channel and forms a 0.99 Å OH bond, oriented perpendicular to the c-axis (Fig. 5.3a). The calculated geometry is in very good agreement with previous theoretical calculations (Gibbs et al., 2003; Gibbs et al., 2004) and consistent with those inferred from the FTIR results as well (Pawley et al., 1993; Chung and Kagi, 2002). The relaxation of the structure as a result of the defect incorporation is localised and is undertaken mostly by the O atom (~0.12 Å) forming the OH bond. Similar results (i.e. minimal to no distortion of the second and third bonding sphere) have been reported by Ross et al. (2003).

With Li as the charge compensator, we observe larger displacements (i.e. up to 0.17 Å) of the atoms in the nearest neighbor of the defect. Both Al and the Si atoms located across the channel (Fig 5.3b) relax away from their initial positions to increase the size of the channel for accommodating Li. The Li atom keeps its position close to the center of the channel and becomes octahedrally coordinated with six O atoms

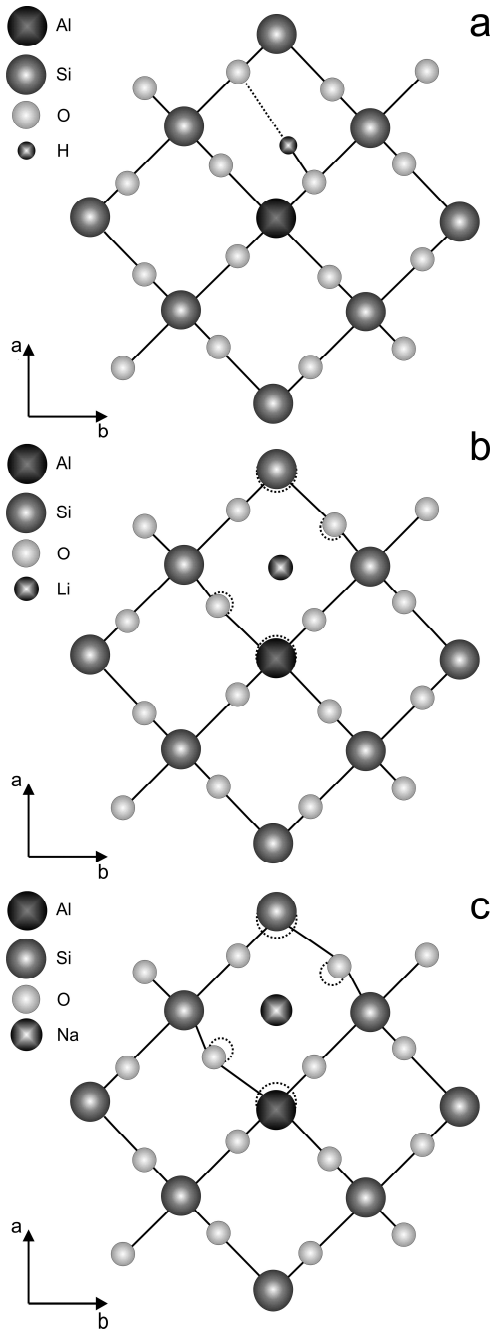

Figure 5.3: Calculated geometries for the diamagnetic $[AlO_6/M]^0$ defects: a) $[AlO_6/H]^0$, b) $[AlO_6/Li]^0$ and c) $[AlO_6/Na]^0$. Comparison between the calculated atom positions in the ideal stishovite structure (dotted circles) and the defective structures (solid circles). Note that only displacements larger than 0.15 Å are shown for comparison.

The charge compensation mechanism involving Na, and resulting in the $[AlO_6/Na^+]^0$ defect (Fig. 5.3b), has an even larger effect on the host structure. Displacements (i.e. up to 0.35 Å) of the atoms surrounding the compensating Na^+ ion are observed, particularly evident in the increased size of the channel. Upon geometry optimisation the Na^+ ion is located close to the center of the distorted channel and is coordinated to six O atoms as well (Fig. 5.3b).

The formation of the $[AlO_6/M^+]^0$ defects in stishovite can be written:

$$M=H^+ \qquad 2Si_xO_{2x} + Al_2O_3 + H_2O \longrightarrow 2Si_{x-1}AlO_{2x}H + 2SiO_2 \qquad (5.1)$$

$$M=Li^+ \qquad Si_xO_{2x} + LiAlO_2 \longrightarrow Si_{x-1}AlO_{2x}Li + SiO_2 \qquad (5.2)$$

$$M=Na^+ \qquad Si_xO_{2x} + NaAlO_2 \longrightarrow Si_{x-1}AlO_{2x}Na + SiO_2 \qquad (5.3)$$

where x depends on the size of the supercell used for calculations (e.g. x=32 for S_{96}). Based on these reactions, the formation energies for the $[AlO_6/M^+]^0$ defects can be calculated. As an example, the formation energy of the $[AlO_6/H^+]^0$ defect can be derived using the following expression:

$$E_{defect}^{formation} = 2*E(Si_{x-1}AlO_{2x}H)+2*E(SiO_2)-2*E(Si_xO_{2x})-E(Al_2O_3)-E(H_2O) \qquad (5.4)$$

The energies of Al_2O_3, H_2O and SiO_2 (stishovite) have been calculated using the computational parameters described above. The defect formation energies for $[AlO_6/Li^+]^0$ and $[AlO_6/Na^+]^0$ can be calculated in an analogous manner. Specifically, the energy calculations for Al_2O_3, $LiAlO_2$ and α-$NaAlO_2$, started from the experimental lattice parameters reported by Ishizawa et al. (1980), Marezio and Remeika (1966) and Reid and Ringwood (1967), respectively, and their structures were optimised using the computational parameters mentioned above. The calculated energies for the formation of $[AlO_6/M^+]^0$ are 0.64 eV, 2.17 eV and 10.15 eV for $M=H^+$, Li^+ and Na^+ respectively. We

emphasize that these formation energies are for removing the Si atom to infinite distance above the surface and that these values should be halved if Si is displaced only to the surface (Ottonello et al. 1990).

5.4 Discussions and Conclusions

5.4.1 $[AlO_6]^0$ paramagnetic center and comparison with previous theoretical calculations

Tani (2000) performed molecular orbital calculations for the Al, Ti and Ge centers in stishovite by the discrete variational (DV)-Xα method for a $S_{11}O_{44}$ cluster. His results support the localization of the unpaired spin in the 3d-orbital for the Ti center and in the 4s-orbital for the Ge center (which has not been detected by EPR), hence $[TiO_6]^0$ and $[GeO_6]^0$ type electron centers. His calculations showed that the trapped hole in the Al center, different from the Ti and Ge centers, does not occupy any orbitals of the Al atom but resides in the oxygen 2p-orbitals surrounding Al, and suggested it to be consistent with the model proposed by Ogoh et al. (1996a). We emphasize that Tani (2000) was not explicit about the location of the unpaired electron on two or six oxygen atoms, only the former would be consistent with the model proposed by Ogoh et al. (1996a). Our calculations have shown that the spread distribution of the unpaired spin among six neighboring oxygen atoms is similar to the problem encountered in the $[AlO_4]^0$ center in quartz, which is attributable to inadequate functionals (To et al., 2005).

Also similar to the $[AlO_4]^0$ center in quartz, the $[AlO_6]^0$ center in stishovite is detectable by EPR only at cryogenic temperatures. Hole hopping between a pair or all four oxygen atoms has been proposed to be responsible for line broadening (and hence

undetectable) of the $[AlO_4]^0$ center in quartz at elevated temperatures. A similar mechanism (i.e., hole hopping among the four equatorial oxygen atoms or all six oxygen atoms) may also be responsible for the detection of the $[AlO_6]^0$ center in stishovite at cryogenic temperatures only.

5.4.2 Implication for incorporation of Al and H in stishovite

Considered to be one of the most important participants in the water transport to the deep lower mantle (Litasov et al. 2007), stishovite is a mineral that has gained tremendous attention during the past two decades due to its wide pressure-temperature stability and ability to retain structurally bound water (as hydroxyl ions) at elevated temperatures and pressures. For examples, Pawley et al (1993), first showed that stishovite, and in particular its Al-bearing variety can contain significant amounts of water (up to 844 wt. ppm H_2O). Subsequently, there have been a number of studies that investigated the effects of minor elements (i.e. Al and H) on the density, phase transition pressure, compressibility (Panero 2006) and elasticity (Panero & Stixrude 2004, Lakshtanov et al. 2007) of stishovite.

Several charge compensation mechanisms have been proposed for the Al incorporation in stishovite. However, the difficulty of the experimental approaches due to the limited crystal sizes and compositional variations for synthetic stishovite makes the interpretation of the experimental data challenging. Indeed there have been limited experimental data available about the local structure environments of Al in stishovite (Ogoh et al. 1966a; Stebbins et al 2006). The first substitution mechanism proposed by

Pawley et al (1993), which has since been supported by both experimental and theoretical studies, is:

$$Si^{4+} \rightarrow Al^{3+} + H^{+} \quad (5.5)$$

However, despite the agreement that exists related to this charge compensation mechanism, the Al/H coupled substitution alone cannot explain the high Al/H values (up to ~7, Litasov et al 2007) measured in synthetic Al-rich stishovite. A second reaction mechanism that involves the presence of an oxygen vacancy was proposed (Pawley et al. 1993):

$$2Si^{4+} \rightarrow 2Al^{3+} + V_O^{2+} \quad (6.6)$$

and previous studies (Panero & Stixrude 2004, Stebbins et al. 2006, Panero 2006) have pointed to the competing roles of the hydrous (5.5) and anhydrous (5.6) substitutions. Stebbins et al. (2006) reported ^{27}Al MAS NMR results for stishovite, found no significant evidence for the presence of O vacancies in the close vicinity of Al, but confirmed the presence of H^{+} as the main charge compensator. In contrast with the experimental results of Stebbins et al. (2006), theoretical calculations by Panero (2006) concluded that the anhydrous substitution could be favoured, explaining thus the Al/H values observed experimentally. However, Litasov et al. (2007) suggested that the high Al/H values can not be explained by these previously proposed reaction mechanisms (5.5 and 5.6) and proposed a third reaction mechanism via the formation of interstitial Al defects:

$$3Si^{4+} \rightarrow 3Al^{3+} + Al_i^{3+} \quad (5.7)$$

However, neither experimental nor theoretical evidence supporting this mechanism exists in the literature.

Our theoretical calculations show that the diamagnetic $[AlO_6/M^+]^0$ defects in stishovite are stable, providing a new substitution mechanism for the incorporation of Al in stishovite.

$$Si^{4+} \rightarrow Al^{3+} + Li^+/Na^+ \quad (5.8)$$

To the best of our knowledge, analytical data for trace elements such as Li and Na are lacking in both natural and synthetic stishovite. However, elevated Li and Na contents in the lower mantle have been suggested from both analysis of mineral inclusions in diamond and high-pressure experiments (e.g. Kesson and Gerald, 1992; Seitz et al., 2003; Hirose et al., 2004; Akaogi, 2007). Therefore, alkali trace elements may play a significant role in the incorporation of Al in stishovite in the lower mantle.

5.5 References

Akaogi M (2007) Phase transitions of minerals in the transition zone and upper part of the lower mantle. GSA Special Paper 421: 1-13

Alfredsson M, Brodholt JP, Wilson PB, Price GD, Cora F, Calleja M, Bruin R, Blanshard LJ and Tyer RP (2005) Structural and magnetic phase transitions in simple oxides using hybrid functionals. Molecular Simulations 31: 367-377

Alvarez JR, Rez P (1998) Electronic structure of stishovite. Solid State Communication 108: 37-42

Barker (1975) Hyperfine parameters of the Al center in smoky quartz. J Phys C: Solid State Physics 8: L142-L144

Becke AD (1988) Density-functional thermochemistry. III The role of exact exchange. Journal of Chemical Physics 98: 5648-5652

Bill H (1969) Investigation on colour centres in alcaline earth fluorides. Helvetica Physica Acta 42: 771-797

Bromiley GD, Bromiley FA, Bromiley DW (2006) On the mechanism for H and Al incorporation in stishovite. Physics and Chemistry of Minerals 33: 613-621

Botis SM, Pan Y (2009) Theoretical calculations of $[AlO_4/M^+]^0$ defects in quartz and implications for the uptake of Al. Mineralogical Magazine (*accepted for publication*)

Botis SM, Adriaens DA, Pan Y (2009) Ab initio calculations on the O_2^{3-}-Y^{3+} center in CaF_2 and SrF_2: its electronic structure and hyperfine constants. Phys Chem Miner 36:1-7

Chung JI, Kagi H (2002) High concentration of water in stishovite in the MORB system. Geophysical Research Letters 29: 16

Cora F, Pisani C (1994) A quantum-mechanical *ab-initio* simulation of neutral and charged point-defects in alpha-quartz. Modelling and Simulation in Material Science and Engineering 2: 965-974.

Devine RAB, Hubner K (1989) Radiation-induced defects in dense phases of crystalline and amorphous SiO_2. Physical Review B 40: 7281-7283

Dickson RS, Weil JA (1990) The magnetic properties of the oxygen-hole aluminum centres in crystalline SiO_2. IV. $[AlO_4/Na^+]$. Canadian Journal of Physics 68: 630-642

Dovesi R, Ermondi E, Ferrero E, Pisani C, Roetti C (1983) Hartree-Fock study of lithium hydride with the use of a polarizable basis set. Physical Review B 29: 3591-3600

Dovesi R, Roetti C, Freyria Fava C, Prencipe M and Saunders VR(1991) On the elastic properties of lithium, sodium an potassium oxide. An ab initio study. Chemical Physics 156: 11-19

Dovesi R, Saunders VR, Roetti C, Orlando R, Zicovich-Wilson CM, Pascale F Civalleri B, Doll K, Harrison NM, Bush IJ, D'Arco P, Llunnell M (2006) CRYSTAL2006, User's Manual; http://www.crystal.unito.it, University of Torino, Torino

Gibbs GV, Cox DF, Boisen MB, Downs RT, Ross NL (2003) The electron localisation function: a tool for locating favourable proton docking sites in silica polymorph. Physica and Chemistry of Minerals 30: 305-316

Gibbs GV, Cox DF, Ross NL (2004) A modeling of the structure and favourable H-docking sites and defects for the high-pressure silica polymorph stishovite. Physics and Chemistry of Minerals 31: 232-239

Hirose K, Shimizu N, van Westrenen W, Fei Y (2004) Trace element partitioning in Earth's lower mantle and implications for geochemical consequences of partial melting at the core–mantle boundary. Physics of Earth and Planetary Interiors 146: 249-260

Ikeya M (1993) New Applications of Electron Paramagnetic Resonance: ESR dating, Dosimetry and Spectroscopy. World Scientific, Singapore

Ishizawa N, Miyata T, Minato I, Marumo F, Iway S (1980) Structural investigation of alpha-Al_2O_3. Acta Crystallographica B 36: 228-230

Jolly L, Silvi B, D'Arco P (1994) Periodic Hartree-Fock study of minerals: Hexacoordinated SiO_2 and GeO_2 polymorphs. European Journal of Mineralogy 4: 7-16

Keskar NR, Troullier N, Martins JL, Chelikowsky JR (1991) Structural properties of SiO_2 in the stishovite structure. Physical Review B 44: 4081-4088

Kesson SE, Gerald JDF (1992) Partitioning of MgO, FeO, NiO, MnO and Cr_2O_3 between magnesian silicate perovskite and magnesiowustite—implications for the origin of inclusions in diamond and the composition of the lower mantle. Earth and Planetary Science Letters 111: 229–240

Lee C, Yang W, Parr RG (1988) Development of the Cole-Salvetti correlation-energy formula into a functional of the electron density. Physical Review B 37: 758-789

Lakshtanov DL, Litasov KD, Sinogeikin SV, Hellwing H, Li J, Ohtani E, Bass JD (2007) Effect of Al^{3+} and H^{+} on the elastic properties of stishovite. American Mineralogist 92: 1026-1030

Litasov KD, Kagi H, Shatskiy A, Ohtani E, Lakshtanov DL, Bass JD, Ito E (2007) High hydrogen solubility in Al-rich stishovite and water transport in the lower mantle. Earth and Planetary Science Letters 262: 620-634

Mackey JH (1963) ERP study of impurity-related color centers in germanium-doped quartz. Journal of Chemical Physica 39: 74-83

Mackey JH, Boss JW, Wood DE (1970) EPR study of substitutional-aluminum-related hole centers in synthetic α-quartz. Journal of Magnetic Resonance 3: 44-54

Marezio M, Remeika JP (1966) High-pressure synthesis and crystal structure of α-$LiAlO_2$, Journal of Chemical Physics 44: 3143-3144

Merawa M, Labeguerie P, Ugliengo P, Doll K and Dovesi R (2004) The structural, electronic and vibrational properties of LiOH and NaOH: an ab initio study. Chemical Physics Letters 387: 453-459

Mombourquette MJ and Weil JA (1985) Ab initio self-consistent-field molecular-orbital calculations on AlO_4 centers in alpha-quartz. II. Canadian Journal of Physics 63: 1282-1293

Monkhorst HJ, Pack, JD (1976) Special points for Brillouin-zone integrations. Physics Review B 13: 5188-5192

Montanari B, Civalleri B, Zicovich-Wilson CM, Dovesi R (2006) Influence of the exchange-correlation functional in all-electron calculations of the vibrational frequencies of corundum (alpha-Al2O3). International Journal of Quantum Chemistry 106: 1703-1714

Nada R, Catlow CRA, Dovesi R, Pisani C (1990) An Ab-Initio Hartree-Fock Study of alpha-Quartz and Stishovite. Physics and Chemistry of Minerals 17: 353-362

Nilges MJ, Pan Y, Mashkovtsev RI (2008) Radiation-damage-induced defects in quartz. I. Single crystal W-band EPR study of hole-centers in an electron-irradiated quartz. Physics and Chemistry of Minerals 32: 103-115

Nuttall RHJ, Weil JA (1981) The magnetic properties of the oxygen-hole aluminum centers in crystalline SiO_2. II. $[AlO_4/H^+]^+$ and $[AlO_4/Li^+]^+$. Can Journal of Physics 59: 1709-1718

Oganov AR, Brodholt JP (2000) High-pressure phases in the Al_2SiO_5 system and the problem of aluminous phase in the Earth's lower mantle: ab initio calculations. Physics and Chemistry of Minerals 27:430-439

Ogoh K, Yamanaka C, Toyoda S, Ikeya M, Ito E (1994) EPR studies on radiation-induced defects in high pressure phase SiO_2. Nuclear Instruments and Methodes in Physics Research Section B: Beam Interactions with Materials and Atoms 91:331-333

Ogoh K, Yamanaka C, Ikeya M (1995) Hyperfine interaction of electron at oxygen vacancy with the nearest and next-nearest Si-29 in high-pressure-phase SiO_2 – stishovite. Journal of Physical Society of Japan 11: 4109-4112

Ogoh K, Yamanaka C, Ikeya M, Ito E (1996a) Two center model for radiation induced aluminum hole center in stishovite. Journal of Physics and Chemistry of Solids 57: 85-88

Ogoh K, Takaki S, Yamanaka C, Ikeya M, Ito E (1996b) Thermoluminescence and electron spin resonance of atomic hydrogens in coesite and stishovite, high pressure phase of SiO_2. Journal of Physics Society of Japan 65:844-847

Ottonello G, Princivalle F, Della Giusta A (1990) Temperature, composition and f_{O2} effects on intersire distribution of Mg and Fe^{2+} in olivines, Phys. Chem. Min. 17:301-312
Ottonello G, Vetuschi Zuccolini M, Civalleri B (2009) Thermo-chemical and thermo-physical properties of stishovite: An ab-initio all-electron investigation, CALPHAD: Computer Coupling of Phase Diagrams and Thermochemistry, doi:10.1016/j.calphad.2009.01.03

Pacchioni G, Frigoli F, Ricci D, Weil JA (2001) Theoretical description of hole localization in a quartz Al center: The importance of exact electron exchange. Physics Review B 63: 054102

Panero WR (2006) Aluminum incorporation in stishovite. Geophysical Research Letters, 33: L20317

Panero WR, Benedetti LR, Jeanloz R (2003) Transport of water into the lower mantle: Role of stishovite. Journal of Geophysical Research 108: 10

Panero WR, Stixrude LP (2004) Hydrogen incorporation in stishovite at high pressure and symmetric hydrogen bonding in δ-AlOOH. Earth and Planetary Science Letters 221:421-431

Pawley AR, McMillan PF, Holloway JR (1993) Hydrogen in stishovite with implication for mantle water content. Science 261:1024-1026

Reid AF, Ringwood AE (1967) High-pressure $NaAlO_2$, an α-$NaFeO_2$ isotype. Inorganic Chemistry 7: 443-445

Ross NL, Gibbs GV, Rosso KM (2003) Potential docking sites and positions of hydrogen in high-pressure silicates. American Mineralogist 88: 1452-1459

Schweizer S, Spaeth JM (1999) New oxygen hole centres in the x-ray storage phosphor BaFBr. Journal of Physics: Condensed Matter 11: 1723-1733

Seitz HM, Brey GB, Stachel T, Harris JW (2003) Li abundances in inclusions in diamonds from the upper and lower mantle. Chemical Geology 201: 307-318

Sicolo S, Palma G, Di Valentin C, Pacchioni G (2007) Structure and ESR properties of self-trapped holes in pure silica from first-principle density functional calculations. Physics Review B 76: 075121

Stebbins JF, Du LS, Kelsey K, Kojitani H, Akaogi M, Ono S (2006) Aluminum substitution in stishovite and $MgSiO_3$ perovskite: High-resolution ^{27}Al NMR. American Mineralogist 91: 337-343

Tani A. (2000) Radiation-induced defects in quartz and stishovite. Studies of ESR, OSL, TL and MO theory. PhD Thesis

Tani A, Yamanaka C, Ikeya M, Ohtaka O, Katsura T (2000) EPR study of a new electron center in synthetic stishovite, a high pressure polymorph of silica, Applied Magnetic Resonance 18: 559-564

To J, Sokol AA, French SA, Kaltsoyannis N, Catlow CRA (2005) Hole localisation in [AlO_4] defects in silica materials. Journal of Chemical Physics 122: 144704

Yamanaka T, Fukuda T, Komatsu Y, Sumiya H (2002) Charge density analysis of SiO_2 under pressure over 50 GPa using new diamond anvil cell for single crystal structure analysis. Journal of Physics: Condensed Matter 14: 10545-10551

Chapter 6

Conclusion

Major advances attained in the atomic-scale measurements dominate the contemporary scientific climate. New analytical techniques of increased sensitivity are constantly developed and high-energy source facilities are becoming increasingly available to both scientists and the industrial world. In this context, quantum mechanical calculations are becoming an indispensable complimentary tool for understanding the fundamental physics behind the experimental observation and to discriminate between various competing models emerged from the experimental findings.

Making use of quantum mechanical modeling, the present thesis presents results relevant for the fundamental understanding of defect centers in several crystalline systems. The major findings of the present thesis can be summarized as follow:

- The present study presents the first *ab-initio* calculations of the O_2^{3-} type defects in crystalline solids at the DFT level. Our results confirm the stability and the molecular character of the $(O_2^{3-}\text{-}Y^{3+})^0$ center in CaF_2 and SrF_2. The unpaired electron is shown to be almost exclusively localized on and equally distributed between the two oxygen atoms that are separated by a distance of 2.47 Å in CaF_2 and 2.57 Å in SrF_2.

- The present study provides improved results for the geometries and stabilities of the diamagnetic $[AlO_4/M^+]^0$ defects in quartz. Our results show that the structural relaxation arising from incorporation of $[AlO_4/M^+]^0$ defects in quartz depends strongly on the size of the compensating ion and extends beyond the second bonding sphere. Our theoretical results also correctly predict the relative stabilities of $[AlO_4/M^+(a_<)]^0$ defects over their $[AlO_4/M^+(a_>)]^0$ counterparts, as inferred from EPR experiments. In addition, we demonstrate the possible presence of the $[AlO_4/K^+]^0$ defects in quartz. These results provide new insights into crystal-chemical controls on the uptake of Al in quartz.

- The present study evaluates the structural models of $[AlO_4/Li]$ paramagnetic defects in α-quartz. Our results show that three distinct Al-Li paramagnetic defects can be can be found in quartz, two of them having the hole located on a short-bonded O and one trapping the hole on a long-bonded O atom. The present study clarifies the ambiguities related to the structural model of the $[AlO_4/Li]^q$ center and eliminates the uncertainties related to the charge of the compensating Li ion. We also suggest an additional paramagnetic defect $[AlO_4/Li^+(c_{small})]^+$, with the unpaired electron located on a short-bonded O atom and the Li compensator just off the edge of the small channel. However the structural similarities with the $[AlO_4/Li^+(a_>)]^+$ defect would require detection and measurement of the ^{17}O hyperfine structure for an unequivocal EPR identification.

- The theoretical results pertaining to [O_2^{3-}-Al^{3+}] defect in stishovite show that the unpaired spin is 85% localised on one of the six oxygen atoms at an [AlO_6] octahedron, while the calculated ^{27}Al hyperfine constants are similar to those determined by EPR experiments. The present results allows us to propose the Al center in stishovite to represent an $[AlO_6]^0$ defect, and hole hopping among equivalent oxygen atoms is responsible for its detection only at cryogenic temperatures. In addition, the present results show that diamagnetic precursors like $[AlO_6/H^+]^0$, $[AlO_6/Li^+]^0$ and $[AlO_6/Na^+]^0$ are stable in stishovite. The calculated OH bond distance and orientation are in excellent agreement with those inferred from FTIR spectra and previous theoretical calculations. The calculated structure of diamagnetic defects: $[AlO_6/Li^+]^0$ and $[AlO_6/Na^+]^0$ suggest that monovalent cations such as Li^+ and Na^+ are potentially important in accommodating Al in stishovite in the lower mantle.